
Supplementary information

Suspension electrolyte with modified Li⁺ solvation environment for lithium metal batteries

In the format provided by the authors and unedited

SUPPLEMENTARY INFORMATION

Suspension electrolyte with modified Li⁺ solvation environment for lithium metal batteries

Mun Sek Kim,^{1,2,6} Zewen Zhang,^{1,6} Paul E. Rudnicki,² Zhiao Yu,^{2,3} Jingyang Wang^{1,4}, Hansen Wang¹, Solomon T. Oyakhire,² Yuelang Chen,^{2,3} Sang Cheol Kim,¹ Wenbo Zhang,¹ David T. Boyle,^{1,3} Xian Kong,² Rong Xu,¹ Zhuojun Huang,^{1,2} William Huang,¹ Stacey F. Bent,² Lin-Wang Wang,⁴ Jian Qin,² Zhenan Bao² and Yi Cui^{1,5,*}

¹Department of Materials Science and Engineering, Stanford University, Stanford, CA 94305, USA.

²Department of Chemical Engineering, Stanford University, Stanford, CA 94305, USA.

³Department of Chemistry, Stanford University, Stanford, CA 94305, USA.

⁴Materials Sciences Division, Lawrence Berkeley Laboratory, Berkeley, CA 94720, USA.

⁵Stanford Institute for Materials and Energy Sciences, SLAC National Accelerator Laboratory, Menlo Park, CA 94025, USA.

⁶These authors contributed equally: Mun Sek Kim, Zewen Zhang.

*e-mail: yicui@stanford.edu

TABLE OF CONTENTS

| | |
|--|-----------|
| SUPPLEMENTARY FIGURE CAPTION | 3 |
| Supplementary Figure Caption 1 Fig. 1a..... | 3 |
| Supplementary Figure Caption 2 Fig. 1b..... | 3 |
| SUPPLEMENTARY NOTES | 4 |
| Supplementary Note 1 SEI formation hypotheses for Li ⁰ anode..... | 4 |
| Supplementary Note 2 The SEI evolution of the conventional liquid electrolyte..... | 5 |
| Supplementary Note 3 The SEI evolution of the suspension electrolyte..... | 6 |
| Supplementary Note 4 Structural analyses of RCE-SEI and SCE-SEI..... | 6 |
| Supplementary Note 5 Surface energy of the SEI components..... | 7 |
| Supplementary Note 6 DFT calculation of Li adatom binding sites on Li ₂ O (111) surface..... | 8 |
| Supplementary Note 7 Enrichment of fluorinated species near the Li ₂ O surface..... | 8 |
| Supplementary Note 8 Solvation energy measurement..... | 9 |
| Supplementary Note 9 Suspension surface area to volume ratio effect..... | 10 |
| Supplementary Note 10 Correlating the simulation to the solvation energy measurement..... | 11 |
| Supplementary Note 11 Suspension surface area effect..... | 12 |
| Supplementary Note 12 Further ⁷ Li NMR analysis..... | 12 |
| Supplementary Note 13 The suspension electrolyte affected by the suspension contents..... | 13 |
| Supplementary Note 14 The effects of the suspension on Li ⁰ anode..... | 14 |
| Supplementary Note 15 XPS analysis of the elemental ratios..... | 15 |
| Supplementary Note 16 Coulombic Inefficiency decrease percentiles..... | 15 |
| Supplementary Note 17 XPS analysis of the high-performance electrolytes..... | 16 |
| Supplementary Note 18 Electrochemical activity of the Li ₂ O suspension in the electrolyte..... | 17 |
| Supplementary Note 19 Gravity, cell orientation, and suspension migration effects..... | 18 |
| Supplementary Note 20 Understanding the improved electrochemical performances of Li ⁰ | 19 |
| Supplementary Note 21 The suspension effect and future insights..... | 22 |
| SUPPLEMENTARY FIGURES | 24 |
| Supplementary Fig. 1..... | 24 |
| Supplementary Fig. 2..... | 24 |
| Supplementary Fig. 3..... | 24 |
| Supplementary Fig. 4..... | 25 |
| Supplementary Fig. 5..... | 25 |
| Supplementary Fig. 6..... | 25 |
| Supplementary Fig. 7..... | 26 |
| Supplementary Fig. 8..... | 26 |
| Supplementary Fig. 9..... | 27 |
| Supplementary Fig. 10..... | 27 |
| Supplementary Fig. 11..... | 28 |
| Supplementary Fig. 12..... | 28 |
| Supplementary Fig. 13..... | 29 |
| Supplementary Fig. 14..... | 29 |
| Supplementary Fig. 15..... | 29 |
| Supplementary Fig. 16..... | 30 |
| Supplementary Fig. 17..... | 30 |
| Supplementary Fig. 18..... | 31 |
| Supplementary Fig. 19..... | 31 |
| Supplementary Fig. 20..... | 32 |
| Supplementary Fig. 21..... | 32 |
| Supplementary Fig. 22..... | 33 |
| Supplementary Fig. 23..... | 33 |
| Supplementary Fig. 24..... | 33 |
| Supplementary Fig. 25..... | 34 |
| Supplementary Fig. 26..... | 34 |
| Supplementary Fig. 27..... | 35 |
| Supplementary Fig. 28..... | 35 |
| Supplementary Fig. 29..... | 36 |
| Supplementary Fig. 30..... | 36 |
| Supplementary Fig. 31..... | 37 |
| Supplementary Fig. 32..... | 37 |
| Supplementary Fig. 33..... | 38 |
| Supplementary Fig. 34..... | 38 |
| Supplementary Fig. 35..... | 38 |
| Supplementary Fig. 36..... | 39 |
| Supplementary Fig. 37..... | 40 |
| SUPPLEMENTARY TABLES | 41 |
| Supplementary Table 1..... | 41 |
| Supplementary Table 2..... | 42 |
| Supplementary Table 3..... | 43 |
| Supplementary Table 4..... | 43 |
| Supplementary Table 5..... | 44 |
| SUPPLEMENTARY REFERENCES | 45 |

SUPPLEMENTARY FIGURE CAPTION

Supplementary Figure Caption 1 | Fig. 1a

In Fig. 1a, the first subset schematic (leftmost) delineates a projected Li^+ solvation structure that resembles a solvent-separated ion pair (SSIP) of the conventional liquid electrolyte. The dotted lines indicate coordination of a dissociated Li^+ with anion and solvent molecules, in which the dissociated Li^+ is dominantly interacting with solvent molecules that create a strongly solvated Li^+ environment in the conventional liquid electrolyte. The SSIP solvation shell, which is located in the vicinity of Li^0 anode, demonstrates the possible sources to construct SEIs on Li^0 anode. The following subset schematic (centre) shows the SEI formation on Li^0 by reducing solvated Li^+ in the SSIP Li^+ solvation. During the reduction of solvated Li^+ at the surface of Li^0 anode, mostly solvent molecules are dragged along with Li^+ due to strongly coordinated Li^+ with solvent molecules in the SSIP. Then, those dragged solvent molecules in the SSIP Li^+ solvation shell react with Li^0 anode due to high reactivity of Li^0 and get decomposed to form insoluble species that passivate the surface of Li^0 anode. When the solvent molecules start to decompose at the surface of Li^0 anode, there is a decrease in the local solubility near the surface of Li^0 anode, termed as SEI formation region, as the decomposition of polar solvent molecules takes away their ability to dissociate and solvate available species that were in the beginning. The final subset schematic (rightmost) depicts the resulting passivation layer of Li^0 anode composed of compact and indirect SEIs derived from the decomposition of SSIP Li^+ solvation shells in the conventional liquid electrolyte. For the electrolyte with the Li^+ solvation structure of SSIPs, the compact SEI generally has a high organic to inorganic ratio and sparsely distributed indirect SEIs.

Supplementary Figure Caption 2 | Fig. 1b

In Fig. 1b, the first subset schematic (leftmost) delineates a modified Li^+ solvation environment near the Li_2O suspension surface that creates a weakly solvated Li^+ environment, attracts anion/fluorinated species, and adsorbs Li^+ in the suspension electrolyte. As the Li_2O suspension adopts an interfacial interaction mechanism between the surface of Li_2O and its surrounding Li^+ solvation shells, the schematic of the suspension located near the surface of Li^0 is portrayed in purpose. The dotted lines indicate interactions of Li^+ with the Li_2O suspension, anions, and solvents. The following subset schematic (centre) represents the SEI formation on Li^0 with the Li_2O suspension in the electrolyte. The reduction of solvated Li^+ around the Li_2O suspension promotes decomposition of relatively fewer solvents and more anions by dragging the fewer solvents and more anions that are coordinated with Li^+ in the modified Li^+ solvation shell. The reduction of Li^+ in the vicinity of Li_2O suspension is relatively facilitated as the solvated Li^+ becomes weakly solvated around the surfaces of Li_2O suspension. This step also highlights the possible clustering of the partially dissolved Li_2O suspension in the SEI formation region. Despite the Li_2O suspension is almost insoluble in the electrolyte, while maintaining its saturated state in the electrolyte due to its partial solubility, the clustering of the partially dissolved Li_2O suspension into the electrolyte is executed by the decrease in the local solubility around the SEI formation region during the solvent reduction as illustrated in Fig. 1a. The final subset schematic (rightmost) depicts the resulting passivation layer of Li^0 anode composed of compact and indirect SEIs derived from the decomposition of the modified Li^+ solvation shells in the suspension electrolyte. For the suspension electrolyte, the compact SEI has a relatively low organic to inorganic ratio and higher indirect SEI content. Note that the schematics in Fig. 1a,b are not drawn to scale and to exact ratios of components.

SUPPLEMENTARY NOTES

Supplementary Note 1 | SEI formation hypotheses for Li⁰ anode

In general, both chemical and electrochemical side reactions between Li⁰ and electrolyte are responsible for the spontaneous formation of SEI on Li⁰ anode. Due to the high reactivity and low electrochemical potential of Li⁰, an instantaneous chemical reaction among Li⁰ and electrolyte species occurs prior to the electrochemical reaction (unless charge carriers flow instantaneously to Li⁰ in contact with the electrolyte), and the kinetics of the chemical reaction slows down once passivating insoluble compounds form, or SEI formation is completed, at the Li⁰ anode/electrolyte interface¹. The electrochemical side reaction, on the other hand, occurs immediately upon Li⁰ deposition step, causing a reduction of electrolyte species at a negatively charged surface of Li⁰. Although the clear difference between chemically-derived SEI and electrochemically-derived SEI still remains questionable, these two types of side reactions are synchronized and are self-limiting processes that form insoluble species that passivate Li⁰ anode during the battery operation¹.

The SEI evolution is directly linked to the electrolyte, in which the electrolyte Li⁺ solvation structure serves as the predominant factor that presumably dictates the SEI evolutions on Li⁰ anode¹. For instance, the lowest occupied molecular orbital (LUMO) and highest occupied molecular orbital (HOMO) of the electrolyte species in the Li⁺ solvation shells thermodynamically govern the electrochemical reduction (depends on LUMO) and oxidation (depends on HOMO) at the battery electrodes². The energetics allow the preferential reduction of anions in the Li⁺ solvation shells of HCEs and LHCEs (due to lowered LUMO energy level of coordinated anions with the dissociated Li⁺ in the Li⁺ solvation shell) to induce anion-derived SEIs on Li⁰ anode^{1,2}. Furthermore, the strength of Li⁺ coordination with solvents and anions within the Li⁺ solvation shell is also the indispensable factor that affects the SEI evolution^{1,3}. It has been reported that fixing anion and varying solvent molecules (thereby changing Li⁺-solvent coordination) resulted in different characteristics of SEIs, reflecting the change in the Li⁺ solvation environment by varying the solvents^{4,5}. Thereupon, the characteristics of the Li⁺ solvation environments are subject to SEI formations on Li⁰.

Importantly, the solubility trends of fully and/or intermediately reduced/decomposed electrolyte species, which mainly stem from the Li⁺ solvation shells in the electrolyte, influence the SEI compositions. Any of the reduced electrolyte species must be saturated first in the electrolyte, especially around the SEI formation region that is located in the vicinity of Li⁰ anode, in order to initiate the constructions of SEIs⁶ by clustering (equivalent to precipitation but in a smaller scale) and polymerization of insoluble species⁷ derived during the decomposition of species in the electrolyte Li⁺ solvation shells. Since the species that form during the electrolyte decomposition should be soluble to a certain degree in the electrolyte, the solubility trend of decomposed electrolyte compounds could possibly affect the SEI composition. For instance, the solubility trend of Li salts in ethylene carbonate (EC) and dimethyl carbonate (DMC) has been reported as (CH₂OCO₂Li)₂ > LiOCO₂CH₃ > LiOH > LiOCO₂C₂H₅ > LiOCH₃ > LiF > (LiCO₂)₂ > Li₂CO₃ > Li₂O, where Li₂O is least soluble⁸. Li₂O, Li₂CO₃, and LiF (located at the least soluble trend) are apparently the most widely observed inorganics in prevalent SEIs on Li⁰ anode¹. Similarly, lithium ethylene dicarbonate (LEDC), lithium ethylene monocarbonate (LEMC), and lithium methyl carbonate (LMC) organic compounds are known to be almost insoluble and also commonly observed in the prevalent SEIs^{9,10}. Therefore, this leads to the hypothesis that the solubility of inorganic and organic species and the rate of reaching saturation/clustering equilibrium of fully and/or intermediately reduced/decomposed electrolyte species from the electrolyte decomposition may dictate the SEI compositions.

Additionally, the existence of indirect SEIs (SEIs that are located at the compact SEI(the SEI that is directly interfaced with Li^0 surface)/electrolyte interface) has been observed in several studies^{7,11,12}. Indirect SEIs (iSEIs), which have particle-like morphologies and generally form sporadically at the compact SEI/electrolyte interface, have a certain elemental composition (thereby impacting Li^+ migration¹³⁻¹⁶) that depends on the electrolyte formulation⁷. Based on a conventional carbonate electrolyte (i.e., RCE), the elemental composition of the iSEI contains mainly oxygen and fluorine inorganics^{11,12}, resembling $\text{Li}_2\text{O}/\text{LiF}$ conglomerates or O/F containing counterparts¹¹. It has been broadly reported that LiF and fluorine-containing counterparts sustain stabilized interphases on Li^0 anode^{10,11,16}. However, most LiF and fluorine-containing counterparts rarely exist in the compact SEI¹¹, which is primarily composed of Li, C, and O^{10,11,17,18}. From RCE, the presence of nanostructured $\text{LiF}/\text{Li}_2\text{O}$ iSEIs¹¹ was observed, and it has been found that the grain boundary of $\text{LiF}/\text{Li}_2\text{O}$ facilitates Li^+ diffusion by a favoured multiatom hopping mechanism¹⁴. This clearly indicates that the iSEI impacts the transport of Li^+ , implicating the overall Li^+ migration should be affected by the properties of both compact and iSEIs on Li^0 anode. Recently, the composition of iSEIs, interchangeable term of the extended SEI, formed after several days of aging (resting Li^0 anode with electrolytes in the open circuit environment) exhibited Li/C/O/F for LiPF_6 in EC:DEC electrolyte and Li/C/O for LiClO_4 in EC:DEC electrolyte⁷, confirming the composition of the iSEIs is sensitive to the electrolyte formulation.

Supplementary Note 2 | The SEI evolution of the conventional liquid electrolyte

The typical Li^+ solvation structure for the liquid electrolyte (usually dilute electrolyte) comprises of solvent-separated ion pair (SSIP). The SSIP solvation structure preferentially favours the reduction of solvent molecules due to a lowered LUMO energy level of coordinated solvent molecules (meaning LUMO energy level for the uncoordinated solvent molecules is higher) with the dissociated Li^+ in the Li^+ solvation shell¹. We project a decreased solubility region located at Li^0 anode surface, namely the SEI formation region, during the rapid decomposition of polar solvent molecules in the electrolyte that lose their ability to dissociate/dissolve further available electrolyte species that were in the beginning. This phenomenon will eventually facilitate clustering the insoluble compounds in the SEI formation region by promoting a faster saturation of insoluble radical/reductive species⁶ formed during the electrolyte Li^+ solvation shell decompositions. The outcome of this passivation layer from the SSIP solvation structure was observed to yield relatively thick organic-rich compact SEI with very sparsely distributed indirect SEIs^{1,7,10,11,17-19}.

Supplementary Note 3 | The SEI evolution of the suspension electrolyte

The major effect of the Li_2O suspension electrolyte comes from the modified Li^+ solvation environment near the surface of Li_2O . Specifically, the modified Li^+ solvation environment near the Li_2O surface had the following characteristics: (i) dissociated Li^+ became weakly solvated by solvents, (ii) anion/fluorinated species were enriched, and (iii) a strong surface adsorption of Li^+ was observed. This modified Li^+ solvation environment then changes the SEI evolution (Supplementary Note 1) that yields inorganic-rich SEIs on Li^0 anode. Moreover, by adding an inorganic (suspension) that is generally insoluble to electrolyte solvents into a liquid electrolyte to make the suspension electrolytes, the suspension component (i.e., Li_2O) in the electrolyte is always at a saturated state, which possibly makes the suspension component easier to form clusters during the SEI formation. As the solubility trend of inorganics and the rate of the insoluble decomposed electrolyte species reaching the saturation limit in the SEI formation region can affect the SEI evolution (Supplementary Note 2), utilizing Li_2O suspension can possibly address these hypotheses as Li_2O is almost insoluble, but not completely insoluble, in a variety of electrolytes including RCE^{1,11,17,18}. One of the incentives we get by investigating Li_2O suspension is that the effects of Li_2O in the suspension electrolyte can be related to the features of Li_2O in SEIs of Li^0 anode. The working mechanism of Li_2O in the electrolyte is systematically analysed and discussed in detail to confirm the suspension electrolyte design principles and illustrated hypotheses.

Supplementary Note 4 | Structural analyses of RCE-SEI and SCE-SEI

To examine nanostructures of RCE-SEI and SCE-SEI, crystalline and amorphous regions were investigated *via* observing cryo-HRTEM images in Supplementary Fig. 1. Supplementary Fig. 1a shows multi-layered Li_2O in the outer part and mostly amorphous inner part for RCE-SEI, which is in agreement with the previous results using the same electrolyte formulation^{17,18}. For SCE-SEI, the multi-layered Li_2O and Li_2O clusters were distinctively observed (Supplementary Fig. 1b). Since the (80~100 nm in diameter) Li_2O suspension in the electrolyte is too large to be directly incorporated into SCE-SEI (~8 nm), the only two possible ways (Supplementary Fig. 2) of forming Li_2O clusters in SCE-SEI with SCE ($\text{Li}_2\text{O}/\text{LiPF}_6/\text{EC}/\text{DEC}/\text{FEC}$) electrolyte species is through decomposing the oxygen-containing solvent molecules of EC/DEC/FEC, in which the carbon contents should also increase in parallel with the increase in oxygen contents, and/or clustering Li_2O from the partially dissolved Li_2O suspension in the electrolyte. According to Fig. 2g,h and Fig. 4d, SCE-SEI resulted in low carbon content but increased oxygen/ Li_2O content, providing strong evidence of clustering of Li_2O from the Li_2O suspension in the electrolyte. Thus, we hypothesize that the Li_2O clustering in SCE-SEI was allowed by saturating Li_2O in the SEI formation region with SCE that promoted Li_2O clustering during the SEI formation on Li^0 , in which the decreased local solubility region in conjunction with Li_2O saturation in the electrolyte played a role as illustrated in Fig. 1b and Supplementary Note 3.

Supplementary Note 5 | Surface energy of the SEI components

In principle, the high surface energy of SEIs provides stronger molecular attraction between Li^0 /compact SEI interface and thermodynamically requires more energy to create new surfaces, which the high surface energy of SEIs helps to prohibit dendritic/high surface area Li^0 electrodeposition²⁰. Therefore, high surface energy components in SEIs are desired in order to suppress Li^0 dendrite formation and proliferation²⁰. The calculated surface energy and diffusion barriers of prevalent SEI components (Li , Li_2O , LiF , Li_2CO_3 , and LiOH) from the literature²⁰ are shown in Supplementary Fig. 3. Notably, Li_2O has the highest surface energy (3.145 eV per atom) among the other SEI inorganics, and Li_2O is the only component that has higher surface energy than that of Li (2.870 eV per atom). This means that thermodynamically, only Li_2O in SEI would be able to suppress dendritic Li^0 electrodeposition due to the relatively high surface energy of Li^0 itself. Additionally, the diffusion barrier of the SEI components affects the surface diffusion of Li^+ that also impacts Li^+ migration behaviour¹⁶. Albeit the low surface diffusion barrier is often desired promoting stable Li^+ migration^{16,20,21}, Li_2O exhibits the highest surface diffusion barrier (0.319 eV) where the diffusion barrier of Li^0 is about 0.139 eV. This high diffusion barrier of Li_2O was perhaps the major reason why Li_2O was thought to be not as beneficial as LiF ²⁰. However, recent studies demonstrated that the conductivity of Li_2O is almost three orders of magnitude higher than that of Li_2O bulk pellets²², indicating that the actual Li^+ conductivity of Li_2O in the compact SEI is much higher. The chemical potential of Li^0 induces richer interstitial sites that improve Li^+ conductivity, which marks Li_2O SEI as the most conductive SEI compared with LiF SEI and native SEI derived from $\text{LiPF}_6/\text{EC}/\text{DEC}$ electrolyte²². The observed size of Li_2O clusters was ranging from 2 to 3 nm in SCE-SEI (Supplementary Fig. 1). With these small dimensions of Li_2O , it is highly possible for nanoscopic Li_2O clusters in SEIs to conduct Li^+ through the bulk instead of diffusing Li^+ across the Li_2O surfaces. We also show later that SCE derived interphases ($\text{Li}_2\text{O}/\text{inorganic-rich}$) is more ionically conductive and electrochemically stable compared to that of RCE derived interphases ($\text{Li}_2\text{O}/\text{inorganic-poor}$). Due to the higher Li^+ conductivity than the bulk Li_2O pellet of Li_2O enabled by the chemical potential of Li^0 anode, it can be postulated that the high diffusion barrier of Li_2O is not a major factor that determines morphological evolutions during Li^0 electrodeposition, rather the surface energy of the compact SEI components (i.e., Li_2O) is perhaps more correlated with the morphological features of Li^0 electrodeposits (Fig. 1c-d and Fig. 2a-b). For the major indirect SEI components such as LiF and O/F inorganic counterparts, on the other hand, we speculate that the diffusion barrier plays a more significant role to regulate stable Li^+ migration across SEIs on Li^0 anode, as not only LiF and fluorine inorganic counterparts are indirectly located at the compact SEI/electrolyte interface but also exhibit low Li^+ conductivity^{1,7,22}, in which Li^+ conduction through the bulk is less likely to proceed during the Li^+ migration, thereby the diffusion across the surface is much more favoured. By combining these essential pieces of evidence, we hypothesize that the high surface energy of Li_2O in the compact SEI played an important role to suppress dendritic Li^0 electrodeposition and facilitates better Li^+ migration across the compact SEI on Li^0 .

Supplementary Note 6 | DFT calculation of Li adatom binding sites on Li₂O (111) surface

The binding energy of Li adatom onto a surface site can be calculated by subtracting the sum of the energy of a single Li atom and the energy of the surface site before Li adsorption from the total energy of the surface site after the Li adsorption. Therefore, a more negative binding energy (often referred to as high binding energy) of Li onto a specified surface site means a stronger Li binding onto the specified surface. It is important to note that the absolute magnitude of the Li adatom binding energy onto the Li₂O surface is not too relevant for this study as Li₂O was not considered as the Li⁰ electrodeposition substrate; in addition, the DFT simulation is not well suited for capturing the dynamics of charged ions on the surface (where this is investigated in detail with the MD simulations instead). Therefore, observing the trend of the Li binding energies for the possible Li adsorption sites *via* DFT can reveal the most favoured Li interaction sites relative to the other possible sites available on the specified surface. To extract pertinent information through the DFT analyses, the binding energies of Li adatom onto Li₂O (111) surfaces were calculated. The Li₂O (111) surface was chosen as it was experimentally observed in this study (Supplementary Fig. 1) and is also known to be the dominant surface for Li₂O in general^{17,18}. Based on the simulation output (Fig. 3c), there were a total of three possible Li adatom binding sites that exist for Li₂O (111) surface, in which these sites were demarcated as sites 1, 2, and 3. Sites 1, 2, and 3 refer to the Li adatom adsorbed close to the oxygen on the Li₂O surface, the Li adatom adsorbed to the outward lithium on the Li₂O surface, and the Li adatom adsorbed to the inward lithium on the Li₂O surface, respectively. The calculated binding energies of Li adatom onto sites 1 to 3 are -0.93 eV, -0.10 eV, and -0.31 eV, respectively. The highest binding energy was found to be site 1 in Li₂O (111) surface, indicating that Li adatom tends to interact most favourably with the oxygen in Li₂O (O_{Li₂O}). This important trend implies that the interaction between Li and Li₂O exists, which thermodynamically favours Li to interact with O_{Li₂O}. Hence, combining MD and DFT simulation results, it is expected that Li₂O most likely to impact the Li⁺ solvation environment due to the evidence of observing Li⁺⁰-Li₂O interaction.

Supplementary Note 7 | Enrichment of fluorinated species near the Li₂O surface.

The enrichment of FEC relative to EC was found to arise from improved coordination between the fluorine atom and the oxide surface relative to the hydrogen in the same position in EC (Supplementary Fig. 7). While EC commonly coordinates with the surface in a “head-down” configuration (Supplementary Fig. 7b), in which the carbonyl oxygen (O=C) directly interacts with the Li₂O surface while the remainder of the molecule points away from the Li₂O surface, the observed density peak in the fluorine of FEC at the Li₂O surface corresponds to an increase in surface coordination through additional “flat” and “head-up” configurations (Supplementary Fig. 8). These additional favourable configurations bias the composition near the Li₂O surface towards FEC rather than EC. Notably, while the PF₆⁻ density peak near the Li₂O surface was of similar magnitude to those of the solvents, the average PF₆⁻ composition in the first Li⁺ solvation shell sharply increased, demonstrating a preference for the formation of CIPs and AGGs near the Li₂O surface while SSIPs are dominant in the bulk (away from the Li₂O surface and RCE). These effects lead to an overall enhancement of fluorinated species in the Li⁺ solvation shells near the Li₂O surface.

Supplementary Note 8 | Solvation energy measurement

This potentiometric method, which utilizes the H-cell with symmetric Li^0 electrodes but asymmetric electrolytes, electrochemically probes Li^+ solvation energy/environment of the electrolytes in interest (EL_{test}) relative to the reference electrolyte (EL_{ref}). It has been found that the electrolytes with smaller cell potentials (E_{cell}) represent more positive solvation energy²³. In other words, more positive solvation energy signifies weaker Li^+ -solvent coordination and higher Li^+ -anion coordination in the Li^+ solvation shells of the electrolytes.²³ Furthermore, the SEIs formed on Li^0 electrodes with EL_{ref} and EL_{test} do not contribute to E_{cell} and the solvation energy differences²³. Therefore, the solvation energy measurement allows direct observation of the relative changes in the Li^+ solvation environment of the electrolytes. As we are trying to analyse the relative Li^+ solvation environment between RCE and SCE, which all use the same liquid electrolytes of [1M LiPF_6 in EC:DEC (1:1 v/v) 10vol% FEC], the choices of the reference electrolytes (EL_{ref}) does not matter for the scope of our interests. The EL_{ref} and the salt bridge used in this study were 1 M LiFSI in DEC and 3 M LiFSI in DME:DOL (1:1 v/v). Furthermore, we have figured out that the sensitivity of the solvation energy measurement is not subject to the suspension electrolyte design (insoluble particles in the liquid electrolyte system). The applicability of the characterization technique is particularly important for analysing the suspension electrolyte systems due to the presence of solid particles in a liquid media. This suggests that conventional scattering techniques might not be suitable to characterize the suspension electrolytes closely. Therefore, finding the right characterization methods for the suspension electrolytes would be crucial. The potentiometric solvation energy measurement, thus, stands out to be one of the valuable techniques to characterize the suspension electrolyte. As having the suspensions in the electrolyte does not interfere with the sensitivity of the measurement, high suspension content (20 wt% Li_2O) was chosen to delineate a clear impact of the Li_2O suspension in the electrolyte. Based on the measurements taken from RCE and 20 wt% SCE in Fig. 4a, a clear trend has been observed, exhibiting the smaller E_{cell} and more positive solvation energy for the electrolyte with the Li_2O suspension (20 wt% SCE). The change in the E_{cell} and solvation energy directly indicates that the Li^+ solvation environment changes by the Li_2O suspension in the electrolyte. In addition, the direction of the change (smaller cell potential and more positive solvation energy) afforded by the Li_2O suspension reveals that the dissociated Li^+ in the solvation shells becomes weakly solvated, which also implies facilitated desolvation of solvated Li^+ in the electrolyte in the presence of Li_2O .

Supplementary Note 9 | Suspension surface area to volume ratio effect

To observe the surface area to volume ratio effect of the Li_2O suspension in the electrolyte, the potentiometric solvation energy measurements were taken with the 20 wt% Li_2O SCE nanoparticle and microparticle (Supplementary Fig. 9). It is evident that the lower surface area to volume ratio suspension particle (20 wt% Li_2O SCE microparticle), but equal wt% in the suspension electrolytes, ended up with the smaller magnitude changes of E_{cell} and solvation energies; however, the same trend of the changes was achieved for both suspension electrolytes containing 20 wt% Li_2O nanoparticles and microparticles in the electrolyte. This result demonstrates that the degree of the Li^+ solvation change depends on the interfacial interaction mechanism (the surface to volume ratio of the suspension) of Li_2O with its surrounding Li^+ solvation shells in the electrolyte. It is important to note that the SEIs formed on Li^0 electrodes with E_{Lref} and E_{Ltest} do not contribute to E_{cell} and the solvation energy differences²³. Hence, this measurement supports the impact of the surface area to volume ratio of the Li_2O suspension in the electrolyte. We also show later that the surface area to volume ratio effect was also observed with ^7Li NMR analyses affecting in the same manner (Fig. 4b and Supplementary Fig. 10).

Supplementary Note 10 | Correlating the simulation to the solvation energy measurement

A clear linkage between the theoretical computation and experimental analyses is needed to make robust conclusions. From the simulation results in Fig. 3, three essential features of the Li_2O suspension in the electrolyte were found. First, the Li^+ solvation environment changes near (~ 0.8 nm) the Li_2O surface. This explains that the working mechanism of the Li_2O suspension depends on the interfacial interaction between the surface of Li_2O and its surrounding Li^+ solvation shells in the electrolyte, which highlights the effect of the surface area to volume ratio of the Li_2O suspension. Second, anion/fluorinated species tend to interact favourably with the surface of Li_2O , while it was opposite with solvent. This means that the Li^+ -anion and Li^+ -solvent coordinations were enhanced and reduced, respectively. Third, a strong surface adsorption of Li^+ was observed for the Li_2O in the electrolyte. This was also supported by Fig. 3d, which suggests the favoured interaction between Li and $\text{O}_{\text{Li}_2\text{O}}$. Therefore, thermodynamically favourable $\text{Li}^{+/0}\text{-O}_{\text{Li}_2\text{O}}$ interaction was realized. All these results boil down to the one important feature of the Li_2O suspension in the electrolyte: “ Li_2O modifies the Li^+ solvation environment”. Hence, it is fundamentally necessary to experimentally verify the change in the Li^+ solvation environment in the electrolyte with Li_2O to draw a solid conclusion.

The solvation energy measurements shown in Fig. 4a evidently revealed the change in the Li^+ solvation environment in the electrolyte afforded by Li_2O . Explicitly, 20 wt% Li_2O SCE exhibited lower E_{cell} and more positive solvation energy than those with RCE. These changes indicate that the Li^+ solvation environment was clearly altered by the Li_2O suspension in the electrolyte. This then directly confirms the most important feature of Li_2O : “ Li_2O modifies the Li^+ solvation environment”. Moreover, relatively low E_{cell} and more positive solvation energy trend achieved with 20 wt% Li_2O SCE suggests that the dissociated Li^+ was weakly solvated by solvents (interchangeably means the decrease in Li^+ -solvent coordination) and the Li^+ -anion coordination was enhanced²³. This verifies the second feature of the Li_2O suspension in the electrolyte. Also, the weakly solvated Li^+ , inferring facilitated desolvation of solvated Li^+ in the electrolyte, by the presence of Li_2O in the electrolyte verifies the third feature of Li_2O as the only way (because there were no additional solvating electrolyte species introduced in the 20 wt% Li_2O SCE compared to RCE) to weakly solvate Li^+ is to attract solvated Li^+ to the surface of Li_2O by interfering Li^+ -solvent coordination, indicating the $\text{Li}^+\text{-O}_{\text{Li}_2\text{O}}$ interaction. The direct way to verify the first feature is by observing the relative solvation energy trend by changing the surface area to volume ratio of the Li_2O suspension in the electrolyte. A smaller magnitude change, but changing in the same direction, in E_{cell} and solvation energy was observed with a lower surface area to volume ratio Li_2O suspension (Supplementary Fig. 9). This proves the first feature that the change in the Li^+ solvation environment originates from the interfacial interactions between the surface of the Li_2O suspension and its surrounding Li^+ solvation shells in the electrolyte. Therefore, all the key features observed from the simulations were experimentally verified.

Supplementary Note 11 | Suspension surface area effect

The simulation results (Fig. 3) and the solvation energy measurements (Fig. 4a) demonstrate that the degree of the Li^+ solvation change depends on the surface area of the Li_2O in the electrolyte. To experimentally verify the surface area effect of Li_2O on the Li^+ solvation environment further, ^7Li -NMR was measured with 1~7 wt% Li_2O nanoparticle and microparticle in SCE (Supplementary Fig. 10). The change in ^7Li -NMR peak positions (retrieved from Supplementary Fig. 10a) with respect to the suspension contents of the Li_2O microparticle observed in Supplementary Fig. 10b indicates that the degree of the Li^+ solvation change is linearly proportional to the absolute surface area of the Li_2O suspension in the electrolyte. It is obvious that the surface area of the suspension increases linearly with the number of particles or the weight contents of the suspension in the electrolyte. Therefore, the linear change in the peak shifts, supported by the linear fit R^2 values (Supplementary Fig. 10b), for both of the Li_2O nanoparticles and microparticles further support that the degree of change in Li^+ solvation environment is proportional to the absolute surface area (that is wt%) of the Li_2O suspension in the electrolyte. By comparing ^7Li -NMR peak shift trend of 1~7 wt% Li_2O microparticle with that of 1~7 wt% Li_2O nanoparticle (Supplementary Fig. 10b), different slopes (the change in ^7Li -NMR peak position [that is also the change in Li^+ solvation environment] per wt% of the Li_2O suspension in the electrolyte) were observed. Thus, the linear peak shifts observed with respect to the Li_2O suspension contents in the electrolyte and the different slopes observed by varying the surface area to volume ratio of the Li_2O suspension in the electrolyte represent that the Li^+ solvation change is affected by the absolute surface area and the surface area to volume ratio of the Li_2O suspension in the electrolyte.

Supplementary Note 12 | Further ^7Li NMR analysis

To make sure the observed peaks in ^7Li NMR spectrum stem from the dissociated Li^+ of LiPF_6 instead of Li_2O , 7 wt% Li_2O added in EC:DEC (without any salts) has been measured (Fig. 4b). Considering the low solubility of Li_2O , which is below the detection limit of the solution-state NMR, no visible peak was observed with 7 wt% Li_2O in EC:DEC. To systematically confirm the NMR response, ^7Li NMR spectra of blank EC:DEC, supernatant of 7 wt% Li_2O in EC:DEC, 1-20 wt% Li_2O in EC:DEC are shown in Supplementary Fig. 11. As expected, no visible peaks were obtained. These results confirm that the relative upfield peak shifts observed in Fig. 4b were indeed arising from the dissociated Li^+ from LiPF_6 .

In addition to the observed peaks of the 1~20 wt% Li_2O SCE (Fig. 4b), the peak broadening reflects the characteristics of the suspension electrolyte design. It is evident that the peak broadening results from the inhomogeneity in the magnetic field agitated by the suspension particles in the electrolyte, eventually leading to wider peak widths. This explains that the peak width increases as the suspension contents increases in SCE (Fig. 4b). It is important to note that the peak position should not be affected by the peak broadening as the peak shapes were symmetrical (Fig. 4b).

Supplementary Note 13 | The suspension electrolyte affected by the suspension contents

The dispersity of the suspension in the electrolyte is affected by the suspension contents. Based on the timeline images shown in Supplementary Fig. 12, the Li_2O suspensions settle over time, and the rate at which the suspension settles depends on the suspension particle size. That is, the larger the particles, the faster settlement due to the gravity. We have found that the suspension dispersity is not too uniform above 7 wt% Li_2O SCE using the (80~100 nm Li_2O nanoparticles). This is directly evidenced by the relative Li^+ solvation changes observed in Fig. 4b, where the peak shifts deviate from the linearity above 7 wt% Li_2O . This infers the aggregation of the suspension particles in the electrolyte was facilitated above 7 wt% Li_2O SCE. Since the suspension aggregates should yield a lower surface area than those of the well-dispersed suspensions in the liquid electrolytes, the relative peak shifts steadily with respect to the increase of the Li_2O content, once the formation of the Li_2O aggregates dominate in the suspension electrolyte (Fig. 4d). Therefore, the 7 wt% Li_2O SCE was considered as the optimal suspension content. This effect was also shown in Fig. 4e.

Supplementary Note 14 | The effects of the suspension on Li⁰ anode

Based on the found mechanism (the modification of the Li⁺ solvation environment near the surface of Li₂O) of the Li₂O suspension in the electrolyte (Fig. 3 and Fig. 4a-c), we hypothesize that it is crucial to have the Li₂O suspension in the vicinity of Li⁰ anode to be effective. To test this hypothesis, the CE of Li⁰ with 7 wt% Li₂O nanoparticle in RCE (SCE), 1 wt% Li₂O nanoparticle in RCE (SCE-N), 7 wt% Li₂O microparticle in RCE (SCE-M), RCE, and 0.5 M LiPF₆ in EC:DEC (1:1 v/v) 10 vol% FEC (RCE-d) were measured with Li|Cu cells (Supplementary Fig. 13). According to Supplementary Fig. 13, the CE of Li⁰ was higher with SCE than that with SCE-N, indicating the dependence of the Li⁺ solvation change with respect to the Li₂O suspension content in the electrolyte. Also, the CE of Li⁰ with SCE was higher than that with SCE-M. This supports that the particle size (Supplementary Fig. 9,10b), the surface area to volume ratio, influenced the CE of Li⁰. Since the suspensions laying out in the vicinity of Li⁰ surface, which depends on the particle size and geometry (Supplementary Fig. 14), was another essential factor as hypothesized, the 1 wt% Li₂O nanoparticle suspension (SCE-N) was more effective than the 7 wt% Li₂O microparticle suspension (SCE-M). This directly confirms the hypothesis as the CE of Li⁰ with SCE-N was higher than that with SCE-M (Supplementary Fig. 13), although the Li⁺ solvation change was lower for 1 wt% Li₂O nanoparticle in RCE than that for 7 wt% Li₂O microparticle in RCE (Supplementary Fig. 10b). Therefore, a smaller size as well as a favourable geometry of the suspension particle (Supplementary Fig. 13) that could promote a complete surface coverage of Li⁰ will deliver a more efficient and better effect of the suspension electrolyte for Li⁰ anode. Since the same analogy applies to SEIs on Li⁰ anode, this is why we believe the inorganic-rich SEIs formed on Li⁰ anode substantially improve the electrochemical performance. Moreover, all the suspension electrolytes (SCE-M, SCE-N, and SCE) exhibited higher CE than that of RCE, which does not contain any suspensions in the electrolyte. This result also supports that the saturation of Li₂O in the suspension electrolyte has an effect (Supplementary Note 4, Supplementary Fig. 1,2, and Fig. 2h); however, the Li⁺ solvation mechanism is a more dominant factor based on the trend observed with SCE-M, SCE-N, and SCE. Due to a noticeable peak of Li⁺ near the surface of Li₂O (indicating the strong surface adsorption of Li⁺ on the Li₂O surface) observed in Fig. 3c, it is possible that the Li⁺ concentration in the bulk electrolyte is lowered. To clarify the impact of the decrease of Li⁺ in the bulk electrolyte, the CE of Li⁰ with RCE-d and RCE were measured. Based on the results shown in Supplementary Fig. 13, lowering the Li⁺ concentration in the electrolyte (RCE-d) reduced the CE of Li⁰ compared to the CE of Li⁰ with RCE. Such an effect is widely observed for low Li salt concentration electrolytes.¹ The improved CEs of Li⁰ with the Li₂O suspension in the electrolyte, which could possibly lower the bulk Li⁺ concentration, tells that the possible changes in the bulk electrolyte property were not the contributing factor. Therefore, these the results support the hypothesis that laying out Li₂O suspension near Li⁰ is important.

Supplementary Note 15 | XPS analysis of the elemental ratios

XPS technique has been widely applied to characterize SEIs on Li^0 anode as the technique provides high resolution in the out-of-plane direction (providing more accurate information about the indirect SEI region) but the poor interpretation on the in-plane spatial resolution, which may provide an inaccurate determination of the arrangements and components in the compact SEI region¹¹. This is one of the reasons that XPS analysis alone may not be sufficient enough to clearly determine and analyse the SEIs formed on Li^0 anode, in which the combination of cryo-(S)TEM and XPS allows to provide more accurate information about SEIs on Li^0 anode¹¹. Therefore, XPS has performed on electrodeposited Li^0 with RCE and SCE on top of the cryo-(S)TEM analyses (Fig. 2) to figure out relevant species that could possibly originate from the anion and solvents around the indirect SEIs derived from RCE (RCE-iSEI) and SCE (SCE-iSEI). In RCE and SCE, the existing electrolyte species were LiPF_6 , EC ($\text{C}_3\text{H}_4\text{O}_3$), DEC ($\text{C}_5\text{H}_8\text{O}_3$), and FEC ($\text{C}_3\text{H}_3\text{O}_3\text{F}$) as shown in the inset of Fig. 4d. The elemental ratios of P/C, F/C, F/O, and C/O provide useful information about the relative decomposition between the anion and solvents in RCE and SCE. For more decomposition of anion relative to that of the solvents, higher P/C, F/C, and F/O ratios should be obtained. The P/C ratio is self-explanatory as P and C were the only elements that exist in the salt and solvents, respectively. Despite FEC contains fluorine, there are only one F and three C in FEC, in which F/C should decrease if FEC tends to decompose more dominantly than the anion. Following the same manner, a higher F/O ratio for SCE suggests that there were relatively more anion-derived species than solvent-derived species. Since SCE-SEI exhibited higher Li_2O and lower solvent decomposed species contents compared to that of RCE-SEI (Fig. e-h and Supplementary Fig. 1), a lower C/O ratio is expected for SCE-iSEI. Hence, comparing these elemental ratios observed for RCE-iSEI and SCE-iSEI, the relative decomposition relationship between the anion and solvent molecules as well as the iSEI contents can be understood.

Supplementary Note 16 | Coulombic Inefficiency decrease percentiles

To numerically represent the effectiveness of the CE improvements with the suspension electrolytes considering relatively small CE changes for the high-performance electrolytes, Coulombic Inefficiency (CI) relative decrease in % from the reference (RCE, RFE, and RLHCE) and suspension (SCE, SFE, and SLHCE) electrolytes were calculated (Supplementary Fig. 20). In Supplementary Fig. 20, the lower CI represents better electrolyte performance. To numerically observe the impact of the suspension, relative CI_{avg} decrease percentiles from the reference (RCE, RFE, and RLHCE) to suspension (SCE, SFE, and SLHCE) electrolytes provide more apparent metrics than CE, especially for the high-performance electrolytes. With relative CI_{avg} decrease percentiles, the effectiveness of the suspension electrolytes relative to that of the reference electrolytes was vividly observed. As a higher CI_{avg} percentile decrease represents a better improvement of the electrolyte system, the CI_{avg} decrease percentiles shown in Supplementary Fig. 20 indicate that the improvements were highest for SCE (57.89 %) then SFE (27.08 %) then SLHCE (21.05 %). In this way, the improvements of the suspension electrolytes using the high-performance electrolytes were not insignificant as perceived from the CE analysis (Fig. 5b).

Supplementary Note 17 | XPS analysis of the high-performance electrolytes

XPS analyses were conducted to access the surface features (around iSEIs) of electrodeposited Li^0 with the high-performance electrolytes (RLHCE, SLHCE, RFE, and SFE). The elemental ratios of N/C, S/C, N/O, and S/O (Supplementary Fig. 23) measured from RFE-iSEI and SFE-iSEI indicate more anion-derived species for SFE-iSEI. This was evidenced by the increased ratios of N/C and S/C from SFE-iSEI relative to that of RFE-iSEI. Also, the increased N/O and S/O ratios of SFE-iSEI relative to that of RFE-iSEI further verify the presence of relatively less solvent-derived species for SFE-iSEI. The high-resolution XPS scans of S, C, N, and O (Supplementary Fig. 24) illustrate relatively higher portions of Li_3N and Li_2O for SFE-iSEI compared to that for RFE-iSEI. The same trend of the elemental ratios (increased N/C, S/C, N/O, and S/O ratios for SLHCE-iSEI relative to that for RLHCE-iSEI) was observed for SLHCE-iSEI (Supplementary Fig. 25). The high-resolution XPS scans of S, C, N, and O in Supplementary Fig. 26 also showed relatively more Li_3N and Li_2O for SLHCE-iSEI than that for RLHCE-iSEI. Overall, more inorganic-rich surface features were obtained with SLHCE-iSEI and SFE-iSEI than that with RLHCE-iSEI and RFE-iSEI.

Supplementary Note 18 | Electrochemical activity of the Li₂O suspension in the electrolyte

From the LSV measurements (Supplementary Fig. 30), almost identical current density profiles have been observed for Li|Al cells with RCE and SCE between 3 V and 4.5 V vs. Li/Li⁺. The increased current density observed for Li|Al cells with SCE above 4.5 V vs. Li/Li⁺ could be attributed to oxidizing Li₂O suspension in SCE. Despite the full cells with NMC811 cathode run above the theoretical oxidation potential of Li₂O (3.1 V vs. Li/Li⁺)²⁴, the LSV results suggest that a much higher potential was required to oxidize the Li₂O suspension in the liquid electrolyte. Such effect is likely due to the suspension electrolyte design (dispersed solids in a liquid). It is highly possible that a liquid electrolyte lubrication layer that may inhibit a physical/direct contact between the suspension and cathode covers around the surfaces of the Li₂O suspension in the electrolyte. This suggests that the additional benefit of the suspension electrolyte design is enabling the usage of the inorganics that have lower oxidation potentials with respect to the cathode (i.e., NMC811) operating potentials allowed by the metastability of inorganic suspensions (i.e., Li₂O) achieved from the suspension electrolyte design. Furthermore, in Fig. 6, the suspension electrolytes exhibited improved CEs in the full cells, which operate between 3 V and 4.3 V vs. Li/Li⁺. The improved CEs of the full cells with the suspension electrolytes relative to that with reference electrolytes reveal that the possible oxidation of the Li₂O suspension in the electrolyte was not significant or impacted during the charging up to 4.3 V vs. Li/Li⁺, which was also evidenced from the LSV measurement (Supplementary Fig. 30). As the CEs of the full cells are mainly determined by the evolutions of SEIs on Li⁰ anode, the stable cycling of the full cells with the suspension electrolytes, reported in Fig. 6, demonstrate that the suspension in the electrolyte remains stable and stabilizes the SEI evolution on Li⁰ anode during the full cell cycling.

To closely observe the redox stabilities between 3 V and 4.5 V vs. Li/Li⁺ of Li|NMC811 cells during the charging/discharging processes, the cyclic voltammograms between RCE and SCE (Supplementary Fig. 31) showed noticeable differences. First, the redox potential at which the current density peaks at the very first charging for RCE was relatively located at a higher potential than that for SCE. This suggests that the overpotential for RCE (in other words, the interfacial impedances of the electrodes with RCE) was higher than that for SCE, which agrees with the interfacial impedance analyses (Fig. 4e-g) and facilitated Li⁺ desolvation mechanism of Li₂O (Fig. 4a). Second, the magnitude of the current responses for the full cell with RCE at the first redox potential in the 1st charging cycle is larger than that of the full cell with SCE. This means that a quantitatively larger amount of the charges was spent at the 1st charging for the full cells with RCE compared to the charges spent for the full cells with SCE. This directly indicates that the Li₂O suspension did not participate in the redox reactions between 3 V and 4.5 V vs. Li/Li⁺ in the first and rest of the cycles of the full cells, which also agrees with the LSV measurement in Supplementary Fig. 30. Third, the redox potential location (shifting to a higher potential for the charging process and shifting to a lower potential for the discharging process) and the magnitude of the current response decrease for the full cells with RCE over the cycle. This tells that there were interfacial impedance build-up and capacity loss over the cycles in the full cells with RCE. On the other hand, the redox potentials and the current responses during the charging and discharging processes for the full cells with SCE remained stable over the cycles, which demonstrates stable and reversible electrochemical performances of the full cells with SCE. Hence, these results support the improved electrochemical performances of using the Li₂O suspension electrolyte, in which the Li₂O suspension in the electrolyte does not significantly participate in the redox during the full cell operations up to 4.5 V vs. Li/Li⁺.

Supplementary Note 19 | Gravity, cell orientation, and suspension migration effects

To further investigate the gravity effect, cell orientation effect, and possibility of the Li_2O suspension in the electrolyte blocking the pores of the separator that could lead to an early cell failure, cyclic voltammetry was conducted to address the gravity, the cell orientation, and the possible suspension migration effects of the suspension electrolyte in the full cells. The gravity direction and tested cell orientation are explained in Supplementary Fig. 32a. Based on the three orientations tested, Top/Bottom/Vertical, the cyclic voltammograms for the five cycles in Supplementary Fig. 32b demonstrate that the redox reactions under the charge/discharge processes from 3 V to 4.5 V vs. Li/Li^+ were weakly affected by the cell orientation and gravity. Although the suspensions settle in the suspension electrolyte along the gravity direction, as shown in Supplementary Fig. 12, the injected suspension electrolyte in the cell remained stable. This could be due to a thin suspension electrolyte layer formed between the separator and the electrodes induced by the internal cell pressure. Since the liquid portion of the suspension electrolyte remains in contact with the electrodes and separator, the suspensions are also likely to remain in the same location. Moreover, the roughly approximated pore size ranges of the separator (31 ~ 112 nm), Li_2O nanoparticle size range (60 ~ 191 nm), Li_2O microparticle size range (850 nm ~ 32 μm) were measured to figure out the possible Li_2O suspension migration across the separator (Supplementary Fig. 14). Based on the dimension retrieved in Supplementary Fig. 14 and considering possible Li_2O aggregates in the suspension electrolytes, it is likely that the suspensions cannot pass through the separator. Note that all the electrochemical measurements were taken with the cells having the Li_2O suspension on both sides of the cell electrodes. The stable and reversible electrochemical reactions observed in Supplementary Fig. 31 for SCE and in the full cell performances in Fig. 6 indicate that the suspensions were not blocking the pores of the separators to cause the early cell failure during the cell cycling. As the suspension nanoparticles were dispersed by the liquid electrolyte prior to the cell assembly, a liquid electrolyte lubrication layer that may inhibit direct contact between the suspension and separator is covering the suspension nanoparticles. This may help to prevent blocking the pores of the separator with the suspension particles in the electrolyte, suggesting one of the potential benefits of the suspension electrolyte design.

Supplementary Note 20 | Understanding the improved electrochemical performances of Li⁰

Based on the theoretical and empirical analyses of the Li₂O suspension electrolyte, the summary of the roles played by Li₂O is provided below to delineate the improved electrochemical performances of Li⁰ anode with the suspension electrolyte.

•Results from the simulations

- (i) The Li⁺ solvation environment changes in the vicinity of the Li₂O surface – Highlighting the interfacial interaction mechanism between the Li₂O surface and its surrounding Li⁺ solvation shells in the liquid electrolyte.
- (ii) The anion/fluorinated species are preferentially interacting with the Li₂O surface – Highlighting an increase in Li⁺-anion coordination and a decrease in Li⁺-solvent coordination.
- (iii) The dissociated Li⁺ preferentially gets adsorbed onto the surface of Li₂O – Highlighting the existence of Li⁺-O_{Li₂O} interaction that possibly relates to the facilitated desolvation of Li⁺ from the Li⁺ solvation shell.

•Results from the solvation energy measurements

- (i) Relatively low cell potentials (E_{cell}) and more positive solvation energies were obtained with the Li₂O suspension electrolyte – Highlighting the changes in the Li⁺ solvation structure in the presence of Li₂O, which dissociated Li⁺ in the solvation shell becomes weakly solvated by the solvents with the increase of the Li⁺-anion coordination.
- (ii) A different magnitude change, but changing in the same direction, in the E_{cell} and solvation energies was observed with different surface area to volume ratios of the Li₂O suspensions – Highlighting the change in the Li⁺ solvation environment originates from the interfacial interactions between the Li₂O suspension surface and its surrounding Li⁺ solvation shells that vary with the surface area to volume ratio of the Li₂O suspension in the electrolyte.
- (iii) The weakly solvated Li⁺ by solvents and increased Li⁺-anion coordination afforded by the Li₂O suspension should yield reduced solvent-derived and increased inorganic-rich/anion-derived SEIs on Li⁰ anode – Highlighting the impact of the Li⁺ solvation change in the electrolyte on the SEI evolution of Li⁰ anode.
- (iv) As the Li₂O suspension creates a weakly solvating Li⁺ environment, facilitated desolvation of Li⁺ from the Li⁺ solvation shell is expected – Highlighting the possibility of lowering the interfacial impedance in the presence of Li₂O in the electrolyte as well as in SEIs on Li⁰ anode.

•Results from the ⁷Li NMR analyses

- (i) The electron density of the dissociated Li⁺ nuclei changes in the presence of the Li₂O suspension in the electrolyte – Highlighting the changes of the Li⁺ solvation environment with Li₂O in the electrolyte.
- (ii) ⁷Li NMR peaks in the spectrum shift to the upfield direction with respect to the increase in the Li₂O suspension contents in the electrolyte – Highlighting the increase in electron density of the solvated Li⁺ with the Li₂O suspension in the electrolyte that signifies the increased Li⁺-anion coordination and Li⁺-O_{Li₂O} interactions.
- (iii) Linear peak shifts in the upfield direction and different slopes (peak shifts per Li₂O wt%) with respect to the Li₂O suspension contents and the surface area to volume ratios of the Li₂O in the electrolyte were observed, respectively– Highlighting the degree of the Li⁺ solvation change is proportional to the absolute surface area and the surface area to the volume ratio of the Li₂O suspension in the liquid electrolyte.

•Results from the SEM and cryo-(S)TEM

- (i) Bulkier Li^0 electrodeposit morphologies were observed with SCE than that with RCE – Highlighting the Li_2O in the electrolyte inhibits dendritic Li^0 electrodeposition.
- (ii) Inorganic-rich (particularly Li_2O), less solvent-derived, and thin compact SEI on Li^0 electrodeposit was observed for SCE-SEI compared with RCE-SEI. Note that a direct incorporation of the Li_2O suspension into the compact SEI was not observed due to relatively larger length scale of the Li_2O suspensions (31~112 nm) than that of the compact SEIs (<12 nm) – Highlighting the impact of the modified Li^+ solvation environment on and the Li_2O clustering in SCE-SEI.

•Results from XPS analyses

- (i) More anion-derived and less solvent decomposed species were observed in the indirect SEI (iSEI) regions on Li^0 electrodeposits with the suspension electrolytes – Highlighting the modified Li^+ solvation environment with Li_2O impacting the SEI evolutions (inducing inorganic-rich SEIs) of Li^0 anode.

•Results from the electrochemical impedance spectroscopy

- (i) The interphases that Li^0 forms with the Li_2O suspension electrolytes exhibited relatively lower interfacial impedances – Highlighting facilitated Li^+ conduction (preferential adsorption of Li^+ on the surface of Li_2O observed by MD simulations) and desolvation (weakly solvated Li^+ confirmed by the solvation energy measurement) across SEIs afforded by the Li_2O in the electrolyte as well as in SEIs on Li^0 electrode.
- (ii) The decrease of the interfacial impedances for Li^0 electrodes varied with the Li_2O suspension content in the electrolytes (Please note that SEIs on Li^0 are primarily the decomposition product of the Li^+ solvation shells¹) – Highlighting the effect of the Li^+ solvation changes that also reflect the dependence of the relative change in the Li^+ solvation environment with respect to the Li_2O suspension contents (that is the absolute surface area of the Li_2O suspension in the electrolyte) as observed in the potentiometric solvation energy measurements and ^7Li NMR analysis.
- (iii) With the suspension electrolytes, the interphases on Li^0 electrodes relatively became temporally and electrochemically stable – Highlighting the desirable properties of Li_2O and inorganic-rich/anion-derived SEIs on Li^0 with the Li_2O suspensions in the electrolytes.

•Results from the electrochemical performances

- (i) Better capacity retentions and higher CEs were achieved with the suspension electrolytes in the full cells – Highlighting the beneficial properties of the Li_2O suspension in the electrolytes, such as creating a weakly solvated Li^+ environment and preferentially adsorbing Li^+ from the Li^+ solvation shells in the vicinity of the Li_2O (from both Li_2O in the electrolytes and SEIs on Li^0) surfaces that facilitates desolvation of Li^+ from the solvation shell, which lowers the interfacial impedance of Li^0 anode and deriving inorganic-rich/anion-derived SEIs on Li^0 anode that promotes stable Li^+ migration and forming temporally stable interphases on Li^0 electrodeposits over the repeated cycles.

Overall, all the evidence that we harvested from the simulations, ^7Li NMR analyses, cryo-(S)TEM characterizations, XPS analyses, and the electrochemical impedance spectroscopy analyses support the improved electrochemical performances of Li^0 anode with the Li_2O suspension electrolytes as each of the experiments and simulations were interrelated to each other. To further strengthen the correlation between the revealed mechanism of Li_2O and improved electrochemical performances, which are not only reported in this work but also from the previous literature, the outcome of this study in a broader view can be related to the functions of the Li_2O in SEIs on Li^0 as well. SEIs, which are composed of inorganics and organics, on Li^0 are directly exposed to the electrolyte species. This means that the inorganic components, specifically addressing Li_2O in this case, in SEIs are most likely to locally modify the Li^+ solvation environment at the SEI/electrolyte interface. In other words, the Li^+ solvation environment in the bulk electrolyte is different from the Li^+ solvation environment at the SEI/electrolyte interface, in which the inorganic composition of SEIs may dictate the characteristics of the Li^+ solvation environment at the SEI/electrolyte interface, thereby influencing the electrochemical performances of Li^0 anode. For instance, there are plenty of reports that showed improved electrochemical performances of Li^0 anode with the multi-layered Li_2O SEI^{17,18,25,26} and increased contents of Li_2O in SEIs^{17,18,22,25-29} on Li^0 anode; however, these works focused on the methods to derive multi-layered Li_2O SEI and to enrich Li_2O contents in SEIs that enhance the electrochemical performance of Li^0 anode without revealing the actual roles played by Li_2O . Furthermore, the inorganic-rich/anion-derived SEIs are known to be beneficial to and significantly improve the electrochemical performances of Li^0 anode. This suggests that the specific roles played by the inorganic components in SEIs are truly essential to control and understand the electrochemical performances of Li^0 anode, in which the roles played by Li_2O in the electrolyte and SEIs are elucidated in this work by adopting the suspension electrolyte design to explain the electrochemical improvement of Li^0 anode.

Supplementary Note 21 | The suspension effect and future insights

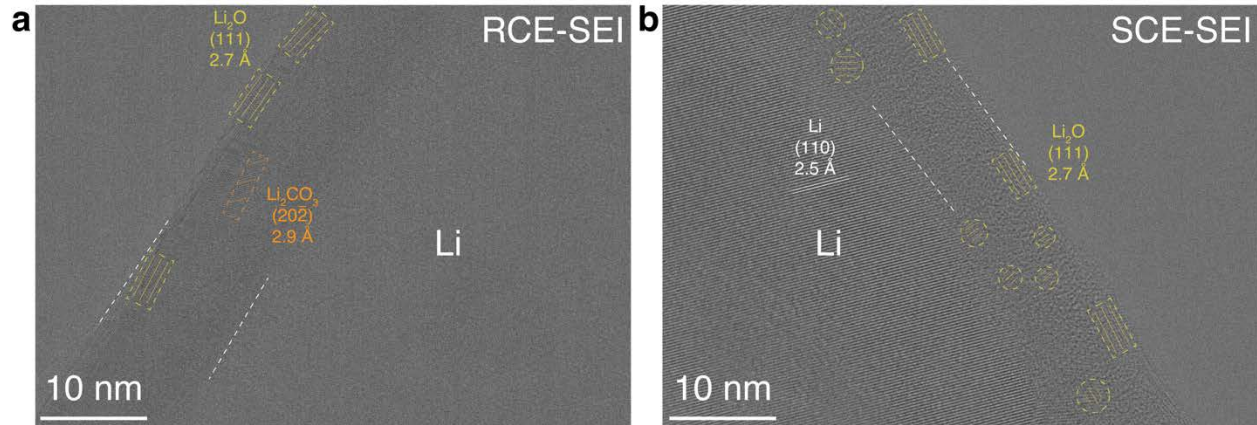
The performance effect of the suspension based on electrolyte systems may vary due to the intrinsic properties of the electrolyte that affect Li^0 anode. For instance, it is known that the conventional carbonate electrolytes create organic-rich or inorganic-poor SEIs on Li^0 anode.¹ On the other hand, high-performance electrolytes^{2-4,30-35} are known to derive inorganic-rich SEIs on Li^0 that largely improve the electrochemical performances of Li^0 anode. Therefore, the magnitude of improving inorganic contents, thereby the electrochemical performances of Li^0 anode, in the SEIs derived from the electrolytes that induce inorganic-poor or inorganic-rich SEIs on Li^0 should vary with the suspension electrolyte design. Considerably, there are also many other factors of the electrolytes, such as Li^+ solvation environments, electrolyte conductivities, dynamics of Li^+ migration at the SEI/electrolyte as well as SEI/electrode interfaces, ..., that could influence the electrochemical performances of LMBs differently with the suspension electrolyte design. Additionally, we speculate that since RLHCE has particular Li^+ solvation that resembles a micelle-like structure (the diluent molecules such as TTE surrounding the CIPs and AGGs¹), $\text{Li}^+-\text{O}_{\text{Li}_2\text{O}}$ interaction perhaps was relatively weakened by the presence of the fluorinated diluent molecules that cover CIPs and AGGs. This important outcome leads to a deeper hypothesis that the suspension electrolytes are more effective (since the suspension adopts the interfacial interaction mechanism) for fully solvating electrolyte system as RCE (single salt and three solvents) and RFE (single salt and solvent) were free of fluorinated diluents. Furthermore, finite elemental analysis has been performed to observe the suspension motions during the cell charging (Supplementary Fig. 36). From the finite elemental analysis, it has been found that the suspensions were not much affected by the electrical field gradient generated by the electrodes, and the elemental analysis implicates that Brownian motion should be the major mechanism that dictates suspension movements in the cell (Supplementary Fig. 36). This leads to an important insight into the size effect of the suspensions as Brownian motion becomes more dominant with smaller-sized particles. We believe that the effect of the suspension electrolytes could be more dramatic with the suspension particles sized below the thickness of SEIs (<10 nm), particularly because this critical suspension size may allow direct incorporation of the suspensions into SEIs during the SEI formation process. Using a smaller dimension of the suspension particles in the electrolyte, therefore, would help to enrich the inorganic contents in SEIs of Li^0 through direct incorporation and would facilitate the suspension particles to be located near the surfaces of Li^0 electrodeposits.

Since the electrochemical performances of Li^0 anode are largely affected by the characteristics of SEIs of Li^0 anode, understanding the dynamics of the inorganics in SEIs are another crucial study to develop LMBs. Although determining solubility trends and limits of inorganics in electrolyte systems is nontrivial and requires constructive/rigorous experiments and simulations⁸, it was qualitatively found that the solubility of the inorganics (i.e., Li_2O , Li_2CO_3 , and LiF)⁸ can be dissolved into electrolyte solvents to a certain degree, in other words, the solubility of inorganics was not zero in electrolyte solvents. This is important as the dynamics of SEI for Li^0 anode depend on the dissolution of SEI species in a particular electrolyte system. Still, specifically proving solubility trends and limits of important inorganics, such as Li_2O , LiF , Li_2CO_3 , Li_3N , and Li_2S , in battery electrolytes would be essential as these inorganics are one of the major constituents of SEIs for Li^0 anode. An important hypothesis is that the dissolution of SEI species may vary based on the electrolytes. Thus, tuning the electrolyte formulation with the suspensions that would promote desirable SEI species to stably remain in SEIs by saturating the desirable inorganics in the electrolyte would be an important future study.

The suspension electrolyte reported is in a nascent stage, which means many other options are available to optimize the quality and performances of the suspension electrolytes, such as optimizing surface area to volume ratio of the suspension particles, synthesizing different geometries of the suspension particles, blending with different types of suspension particles, utilizing suspension friendly electrolyte formulations, and many more. Since the dynamics of the suspensions in the full cell could vary with parameters such as pressure, temperature, C-rates, and electrode geometry, further electrochemical performance optimizations can be considered to develop better suspension electrolytes.

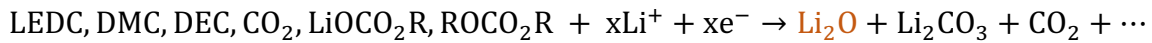
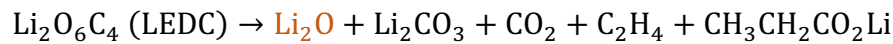
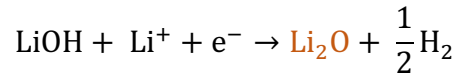
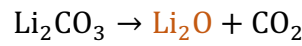
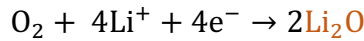
Large-scale applications are also critical. This touches the base of the practicality of the potential use of suspension electrolytes in batteries. Despite making the suspension electrolyte is simple (simply mixing the solids with liquids), many essential parameters such as the feed rates of the suspension into the liquid, mixing techniques, stirring rates, geometries of the mixing propellers and batch containers, filter mesh sizes to sort out the large suspension aggregates, temperatures of the mixing batch and storage containers, and others must be carefully considered for performing the quality controls of the suspension electrolytes with respect to specific suspension particle sizes and types. Conveniently, storing the large quantities of the conventional liquid electrolytes and nanoparticles in a dry atmosphere, which are the only two primary ingredients to make the suspension electrolytes, is already established in the battery manufacturing field. Hence, we believe making the suspension electrolytes is practical. Furthermore, the ways to inject the suspension electrolytes into the battery cell components will be another important aspect for the use of the suspension electrolytes in the batteries. If we consider using the suspension particles that have a larger particle size than the pore size of the separator (meaning the suspension becomes immobile across the battery electrodes), we can create the suspension electrolytes that are specific to the anode and/or cathode. This allows many suspension electrolyte configurations at the cell level. For example, we can apply different types of suspension materials that specifically contribute to the anode and/or cathode sides. Hence, the suspension electrolyte design is a very intriguing system to consider for Li^0 anode with many other cathode materials to construct high-performance batteries. Through our work, we have systematically shown that the suspension electrolyte design is useful for modifying the Li^+ solvation environment and SEI speciation towards stable LMB operations. As a corollary, our approach provides another distinctive pathway towards further developing, studying, and applying a new category of suspension electrolytes in developing electrolytes for LMBs.

SUPPLEMENTARY FIGURES

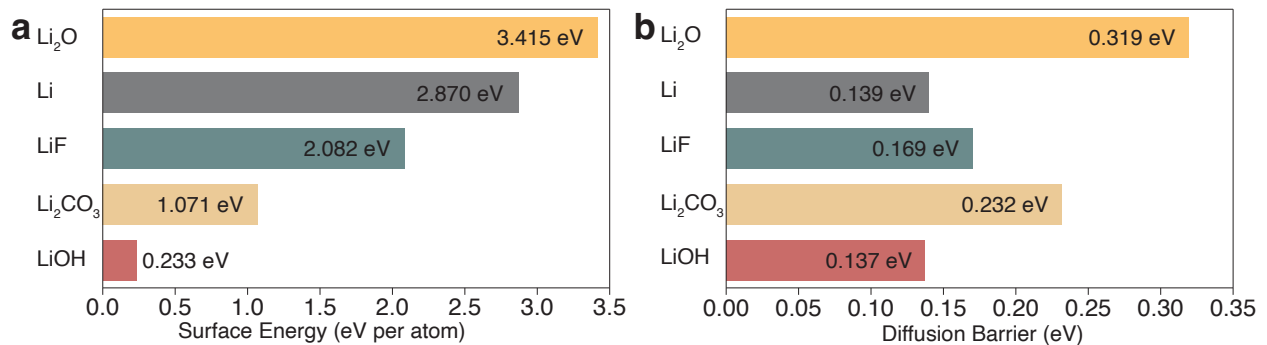


Supplementary Fig. 1. **a**, Cryo-HRTEM image of RCE-SEI on Li^0 anode. The SEI region is designated with the dashed white lines. The lattices for Li_2O and Li_2CO_3 are shown in the inset. **b**, Cryo-HRTEM image of SCE-SEI on Li^0 anode. The SEI region is designated with the dashed white lines. The lattices for Li_2O and Li are shown in the inset.

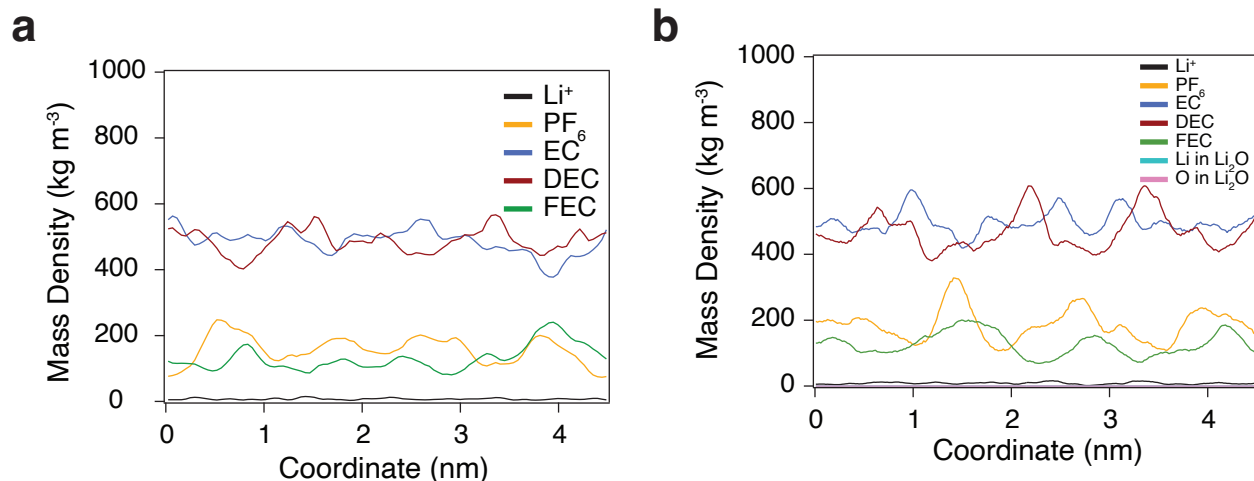
Possible Li_2O formation pathways



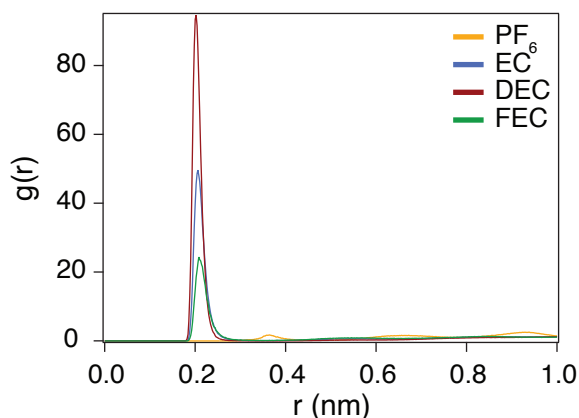
Supplementary Fig. 2. Possible electrolyte species reduction pathways^{8,9,36} to form Li_2O from a conventional carbonate electrolyte.



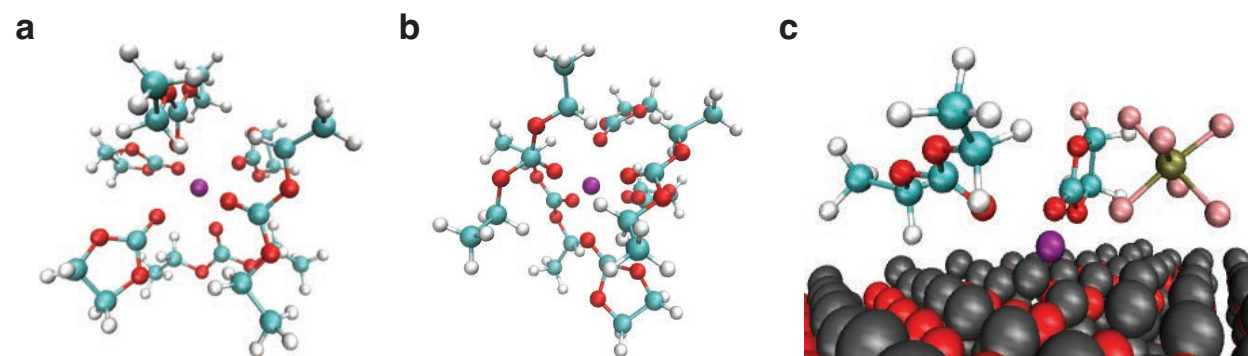
Supplementary Fig. 3. **a**, Literature values²⁰ of the surface energy of Li_2O , Li , LiF , Li_2CO_3 , and LiOH . **b**, Literature values²⁰ of the diffusion barrier of Li_2O , Li , LiF , Li_2CO_3 , and LiOH .



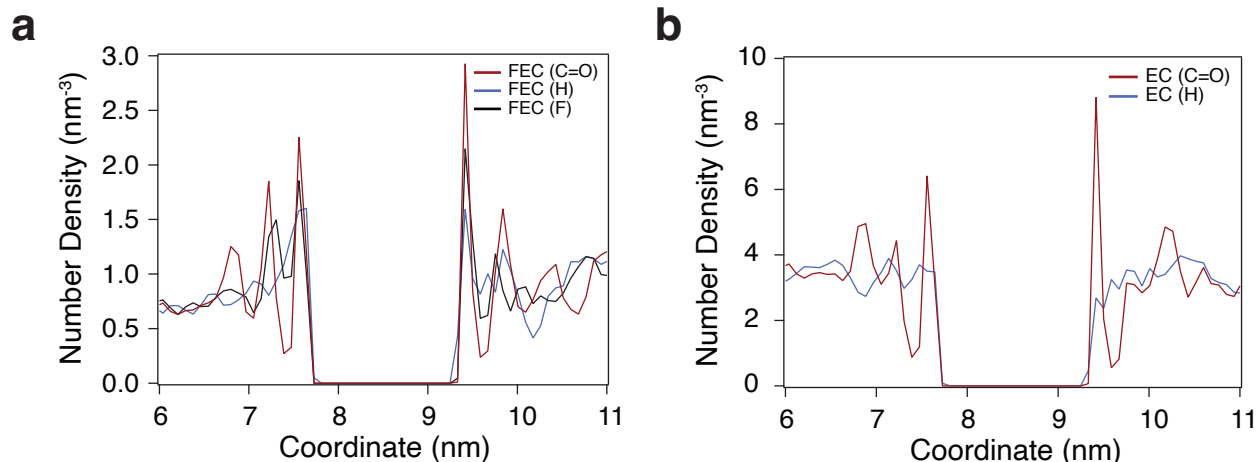
Supplementary Fig. 4. **a**, Density profiles of RCE. **b**, Density profiles of SCE – away from the Li₂O slab.



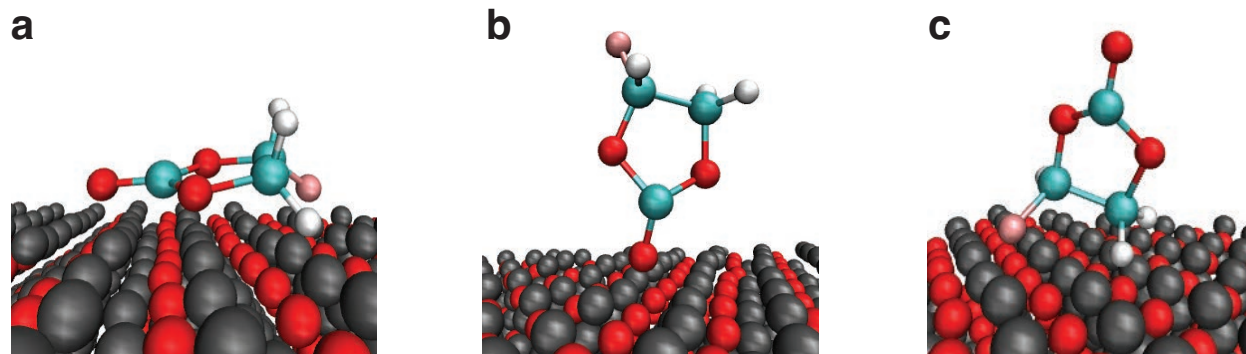
Supplementary Fig. 5. RDFs for the first Li⁺ solvation shell of SCE – away from the Li₂O slab.



Supplementary Fig. 6. Simulated first Li⁺ solvation shells of RCE (**a**), SCE – away from the Li₂O slab (**b**), and SCE – near the Li₂O slab (**c**). The colour codes for the images are Oxygen (red), Carbon (cyan), Hydrogen (white), Phosphorus (tan), Fluorine (pink), Li⁺ (purple), and Li in Li₂O (grey).

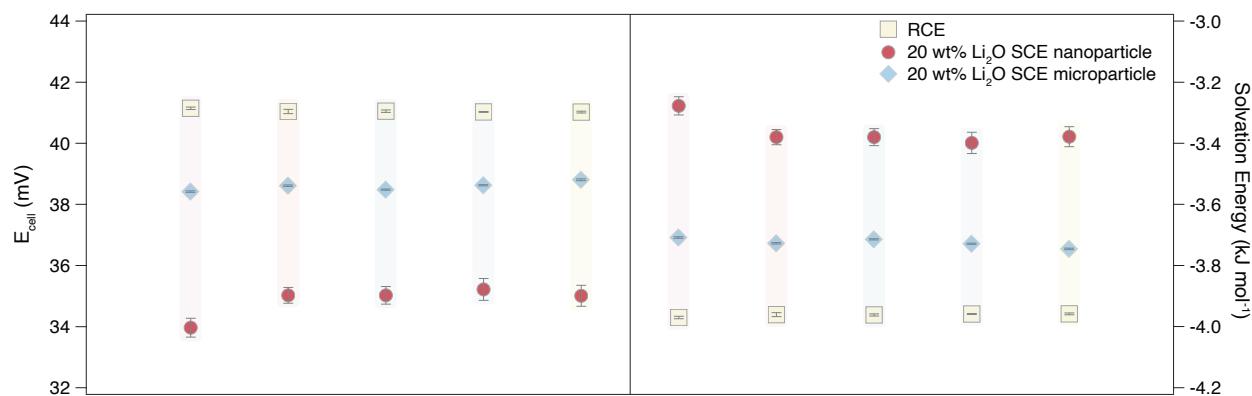


Supplementary Fig. 7. **a**, Density profiles of select atoms in FEC near the Li₂O slab. O=C is the carbonyl oxygen, and F represents the fluorine in FEC. **b**, Density profiles for select atoms in EC near the Li₂O slab. O=C is the carbonyl oxygen, and H represents the hydrogen in the same topological configuration as the fluorine in FEC.

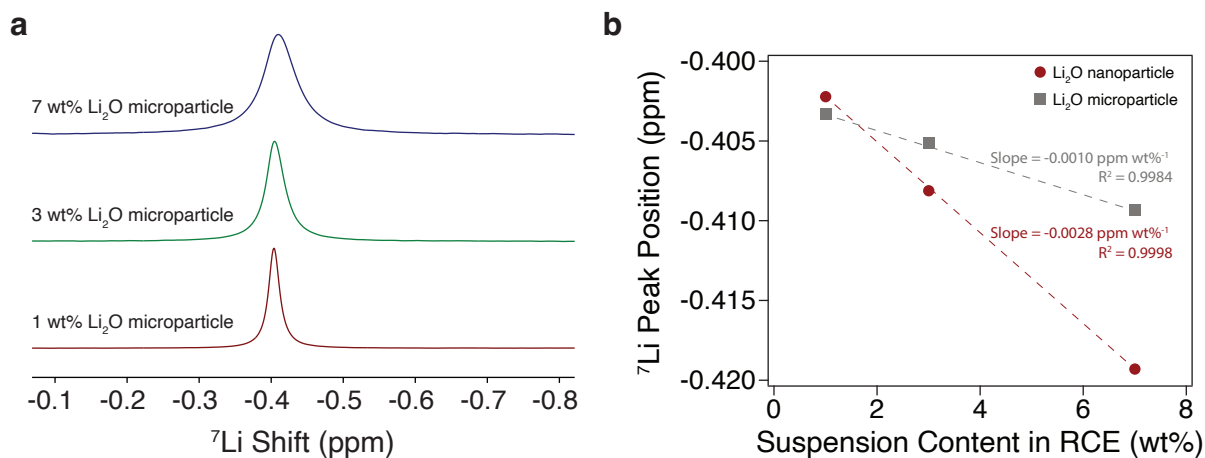


Supplementary Fig. 8. Representative snapshots of FEC coordination structures, “flat” configuration (**a**), “head down” configuration (**b**), and “head up” configuration (**c**), with the Li₂O slab. The carbonyl oxygen is considered as the “head” of FEC. Other molecules are omitted for clarity. The colour codes for the images are Oxygen (red), Carbon (cyan), Hydrogen (white), Phosphorus (tan), Fluorine (pink), Li⁺ (purple), and Li in Li₂O (grey).

Note: Based on Supplementary Fig. 7, the “flat” and “head up” are reasonably favourable configurations for FEC molecules near the Li₂O slab due to the observed peak in fluorine density near the surface, whereas no such peak is observed for the hydrogen in the same position in EC, suggesting that the “head down” configuration is dominant.



Supplementary Fig. 9. The potentiometric measurement of cell potentials (left half) and Li^+ solvation energies (right half) for RCE, 20 wt% Li_2O SCE nanoparticle, and 20 wt% Li_2O SCE microparticle. Five measurements were taken for each of the electrolytes.



Supplementary Fig. 10. **a**, ^7Li -NMR spectrum of SCE with 1 wt%, 3 wt%, and 7 wt% Li_2O microparticles. **b**, ^7Li -NMR peak positions with respect to the suspension contents ranging from 1 wt% to 7 wt% using the Li_2O nanoparticles and microparticles. The ^7Li peak positions for Li_2O nanoparticles were retrieved from Fig. 4b. The dashed lines indicate fitted lines with the slope representing the change in the peak position with respect to the suspension content and R^2 values.

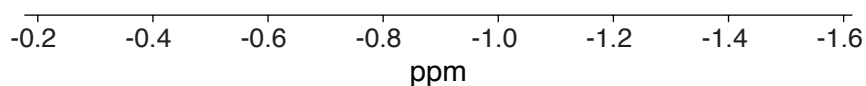
EC:DEC

Supernatant of 7 wt% Li_2O in EC:DEC

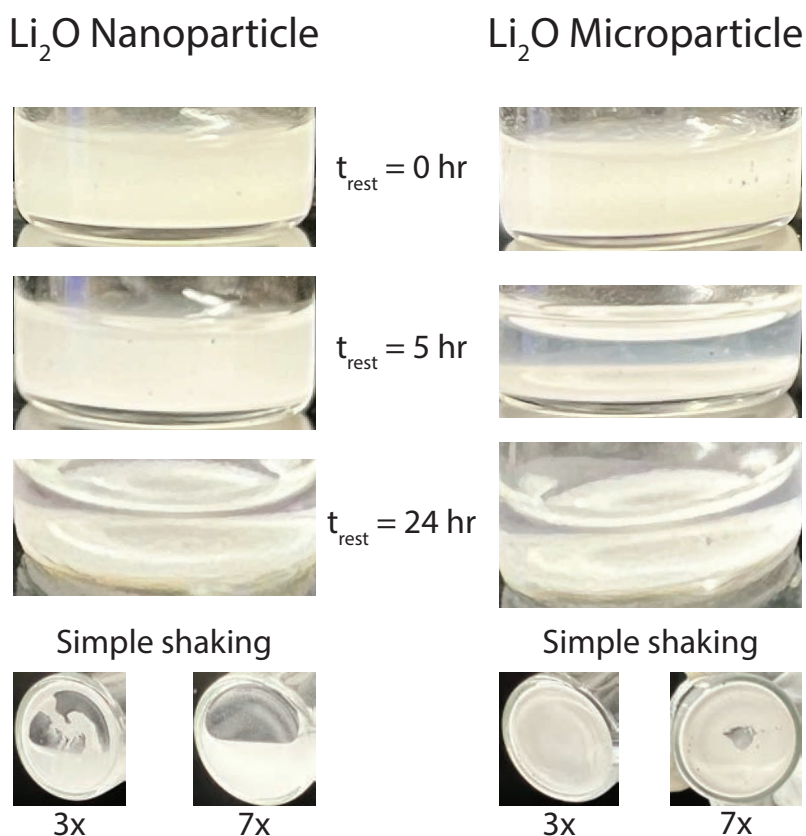
1 wt% Li_2O in EC:DEC

7 wt% Li_2O in EC:DEC

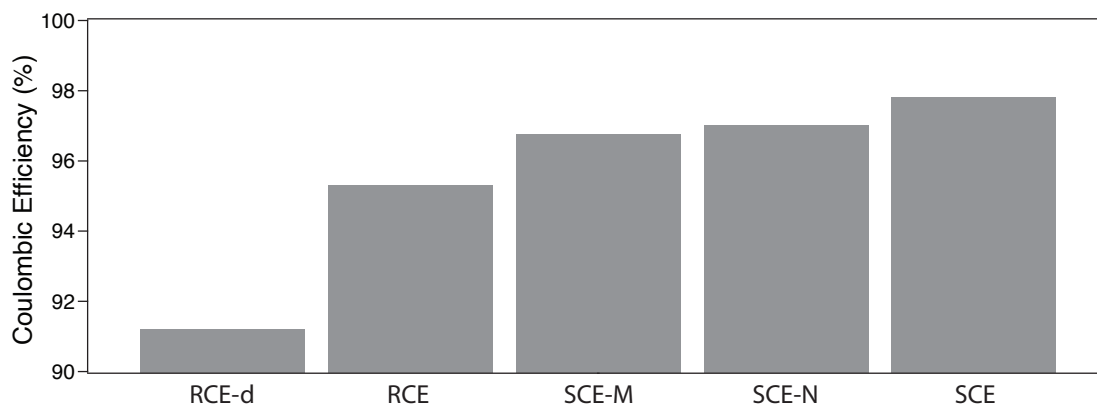
20 wt% Li_2O in EC:DEC



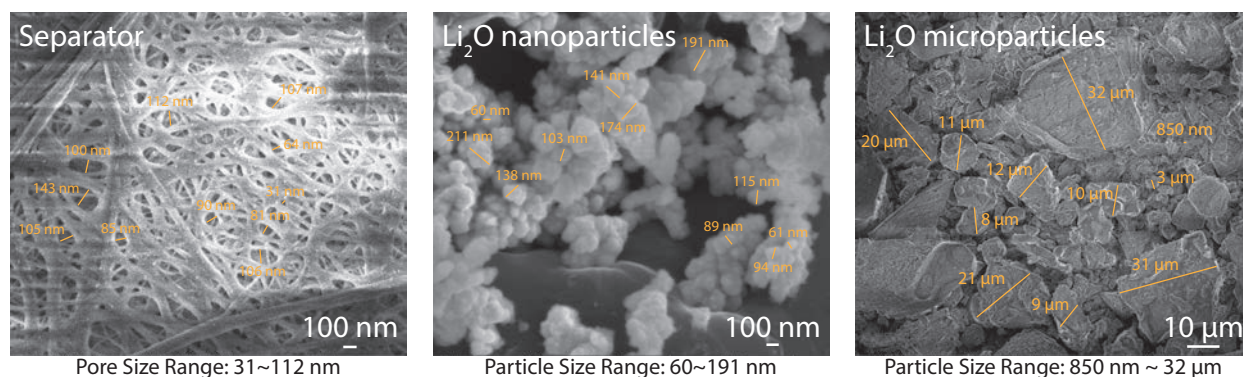
Supplementary Fig. 11. ^7Li -NMR spectrum of the blank solvent composed of EC:DEC (1:1 wt%), the supernatant of 7 wt% Li_2O suspension added into EC:DEC (1:1 v/v), and 1 wt%, 7 wt%, 20 wt% Li_2O suspension added into EC:DEC (1:1 v/v).



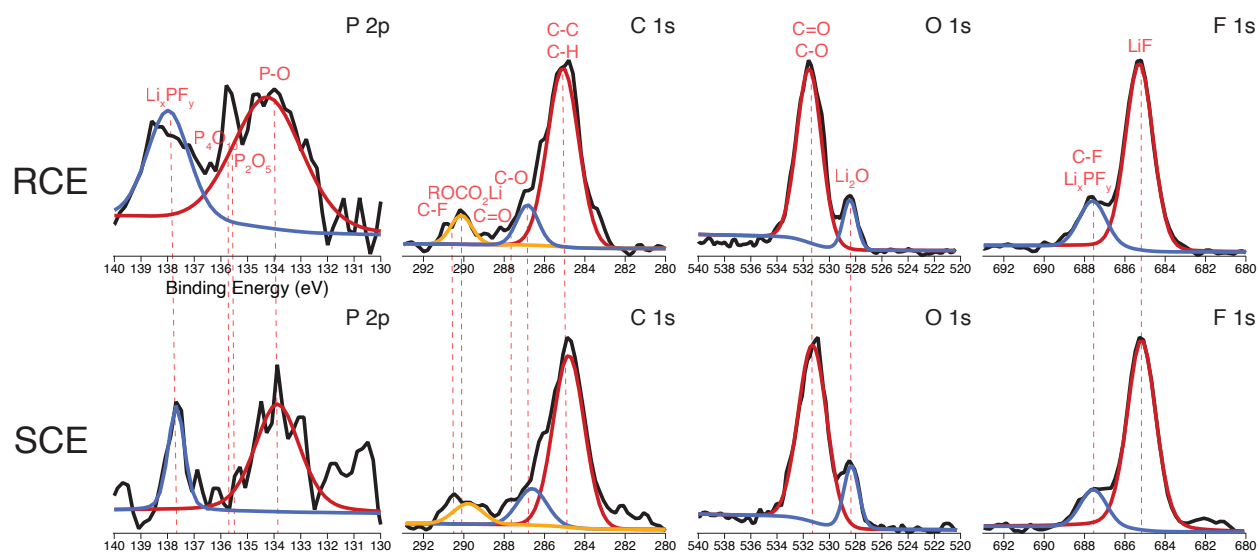
Supplementary Fig. 12. Timeline images of the suspension electrolytes containing 7 wt% of Li_2O nanoparticles or Li_2O microparticles in RCE. The simple shaking is done by hands, and the number represents the shaking the suspension electrolyte after a day by hands three (3x) and seven (7x) times.



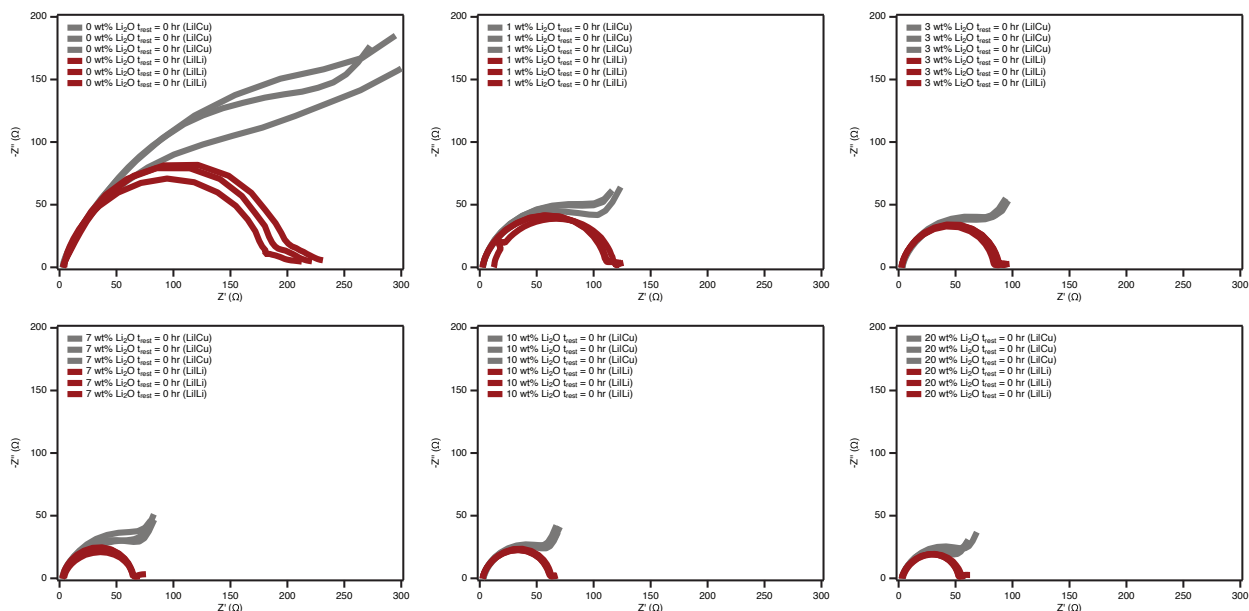
Supplementary Fig. 13. Measured CE from Li|Cu cells with the specified electrolytes. The blends for RCE-d, RCE, SCE-M, SCE-N, and SCE are 0.5 M LiPF₆ in EC:DEC (1:1 v/v) 10 vol% FEC, 1 M LiPF₆ in EC:DEC (1:1 v/v) 10 vol% FEC, 7 wt% Li₂O microparticle in RCE, 1 wt% Li₂O nanoparticle in RCE, and 7 wt% Li₂O SCE.



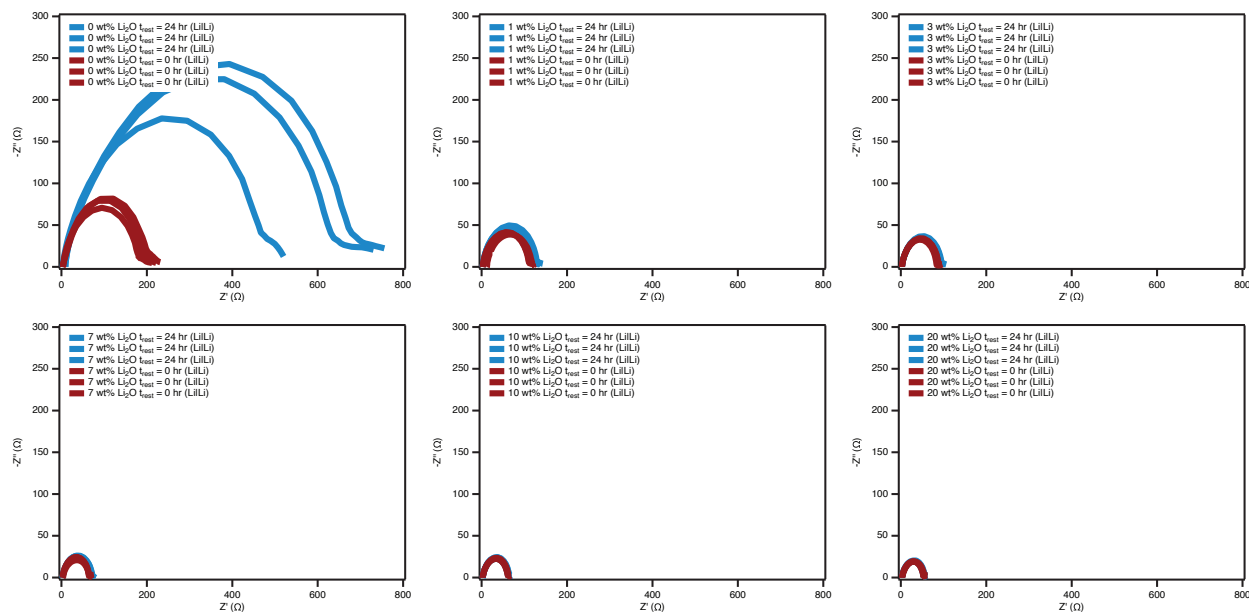
Supplementary Fig. 14. The SEM images of the separator, Li₂O nanoparticle, and Li₂O microparticle used in this study. The size ranges for the separator, Li₂O nanoparticles, and Li₂O microparticles were 31~112 nm, 60~191 nm, and 850 nm~32 μm, respectively.



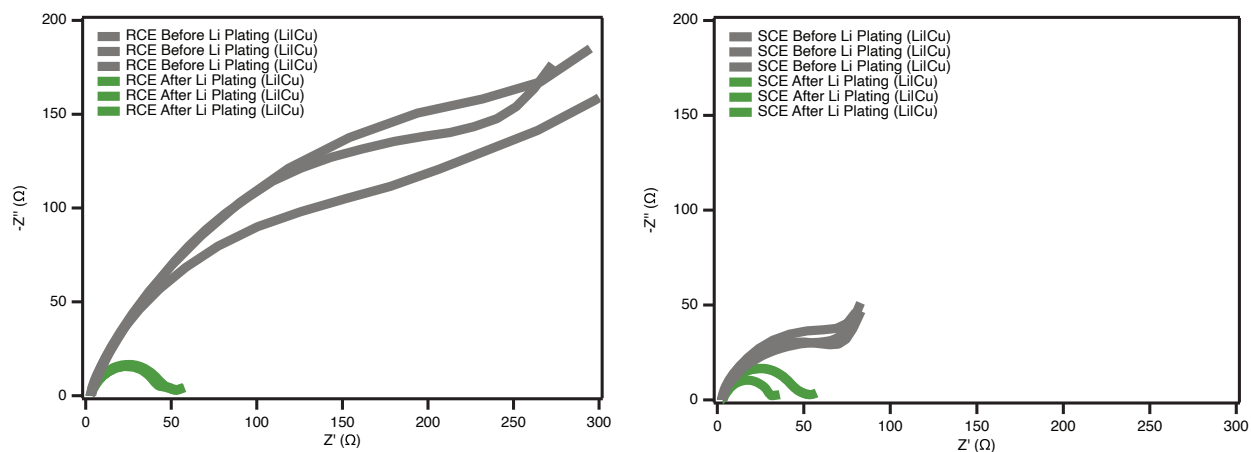
Supplementary Fig. 15. Narrow XPS scans of P, C, O, and F of the electrodeposited Li⁰ on Cu from Li|Cu cells with RCE and SCE.



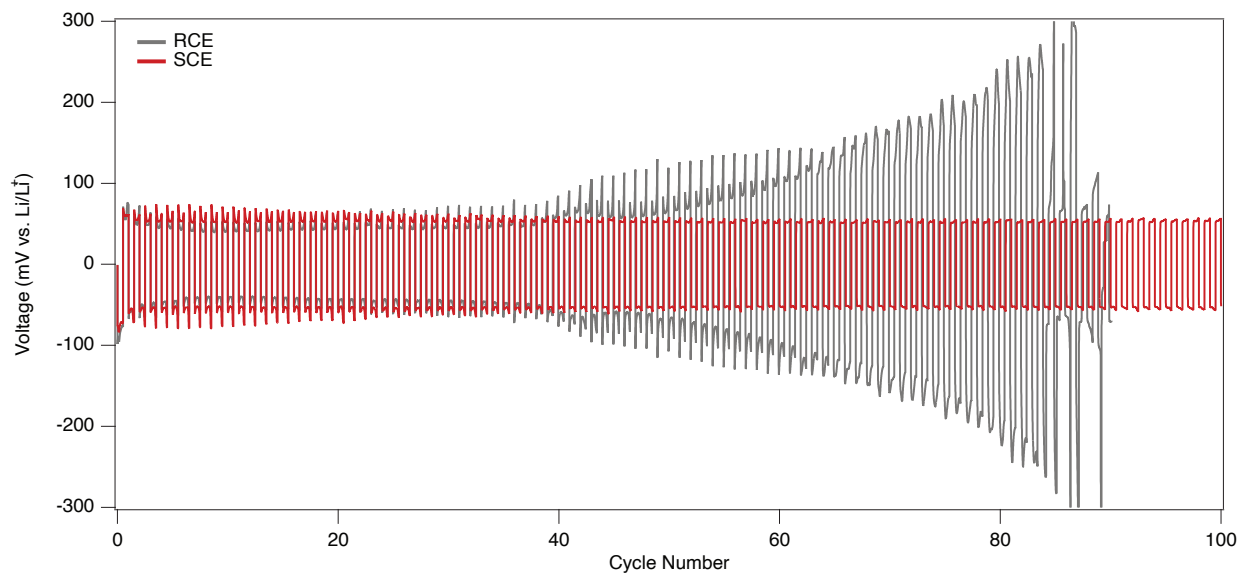
Supplementary Fig. 16. Nyquist plots of three identical Li|Li and Li|Cu cells measured at $t_{\text{rest}} = 0$ hr with the Li_2O suspension content ranging from 0 wt% to 20 wt% in RCE. t_{rest} represents the cell resting time after the cell assembly.



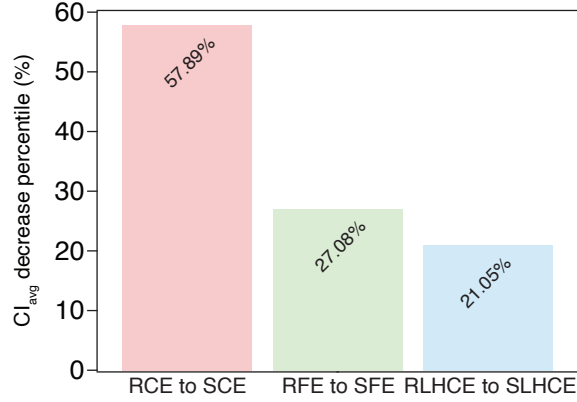
Supplementary Fig. 17. Nyquist plots of three identical Li|Li cells measured at $t_{\text{rest}} = 0$ hr and $t_{\text{rest}} = 24$ hr with the Li_2O suspension content ranging from 0 wt% to 20 wt% in RCE. t_{rest} represents the cell resting time after the cell assembly.



Supplementary Fig. 18. Nyquist plots of three identical Li|Cu cells measured before and after 1 mAh cm⁻² Li⁰ electrodeposited on Cu at 1 mA cm⁻² with RCE and SCE.



Supplementary Fig. 19. Galvanostatic Li plating/stripping voltage profiles of Li|Li cells with RCE and SCE measured at 1 mA cm⁻² and 1 mAh cm⁻².



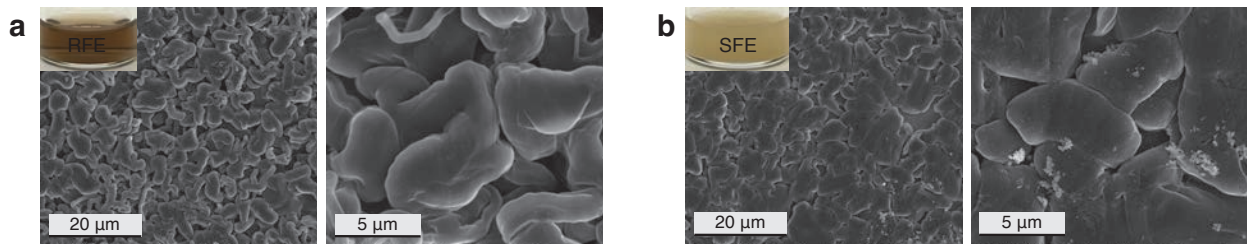
$$CI = 100 - CE$$

$$CI_{decrease}(\%) = \frac{CI_{reference} - CI_{suspension-electrolyte}}{CI_{reference}} \times 100$$

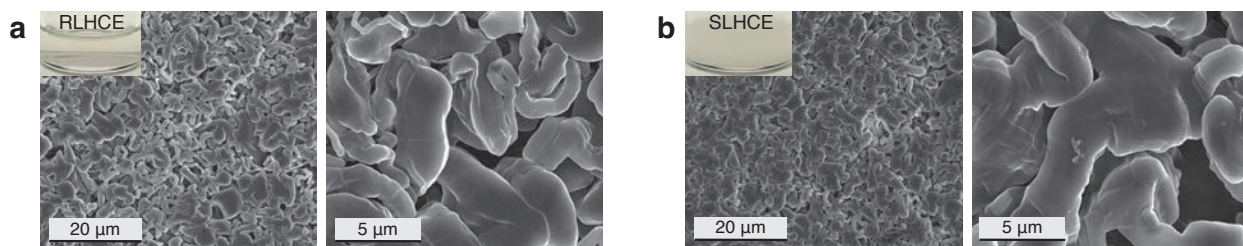
| | RCE | SCE | RFE | SFE | RLHCE | SLHCE |
|-----------------------|-------|-------|-------|-------|-------|-------|
| CE _{avg} (%) | 94.23 | 97.57 | 99.52 | 99.65 | 99.43 | 99.55 |
| CI _{avg} (%) | 5.77 | 2.43 | 0.48 | 0.35 | 0.57 | 0.45 |

| | RCE to SCE | RFE to SFE | RLHCE to SLHCE |
|--------------------------------|------------|------------|----------------|
| CI _{avg} decrease (%) | 57.89 | 27.08 | 21.05 |

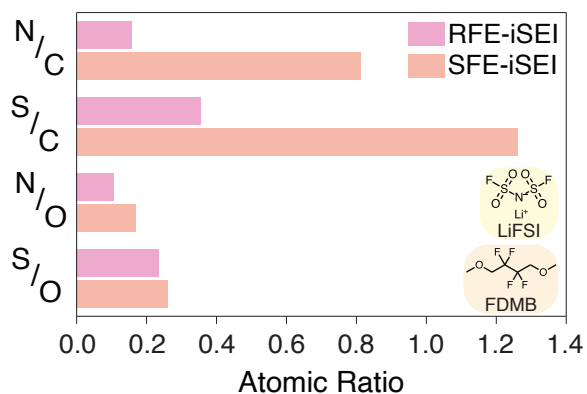
Supplementary Fig. 20. Coulombic Inefficiency relative decrease ($CI_{decrease}$) percentiles from the reference (RCE, RFE, and RLHCE) and suspension (SCE, SFE, and SLHCE) electrolytes. In the equations, CI, CE, $CI_{reference}$, and $CI_{suspension-electrolyte}$ represent Coulombic Inefficiency, Coulombic Efficiency, Coulombic Inefficiency of the reference electrolyte, and Coulombic Inefficiency of the suspension electrolyte, respectively. The averaged CEs (CE_{avg}) were retrieved from Fig. 1d and Fig. 5b.



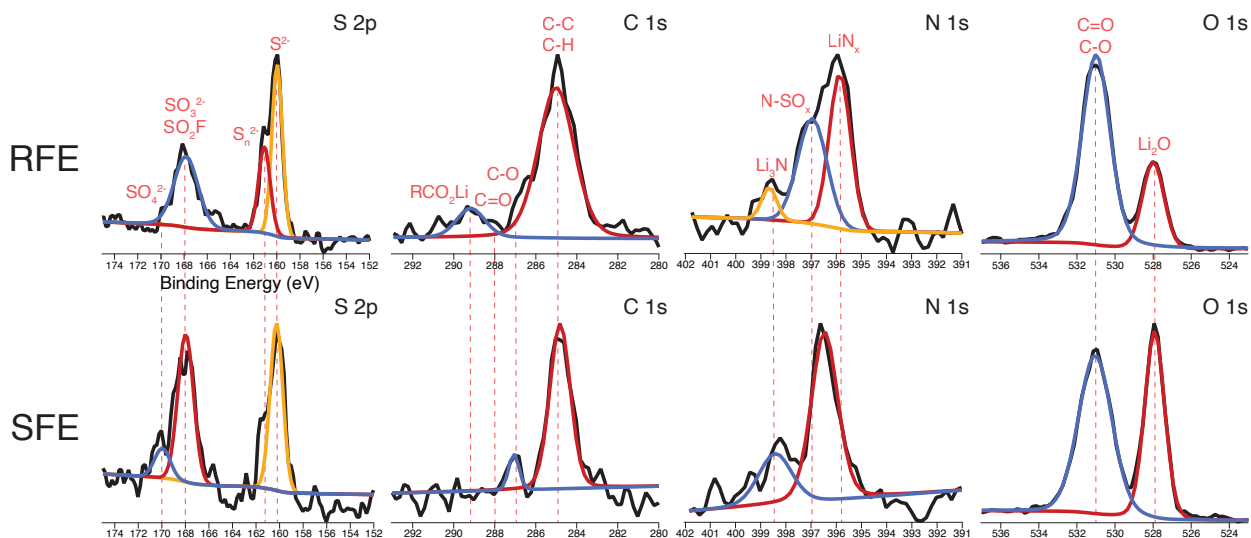
Supplementary Fig. 21. a, Low (left) and high (right) magnification SEM images of electrodeposited Li^0 on Cu with RFE at 1 mA cm^{-2} and 1 mAh cm^{-2} from Li|Cu cell. The inset image shows the physical image of RFE. **b,** Low (left) and high (right) magnification SEM images of electrodeposited Li^0 on Cu with SFE at 1 mA cm^{-2} and 1 mAh cm^{-2} from Li|Cu cell. The inset image shows the physical image of SFE.



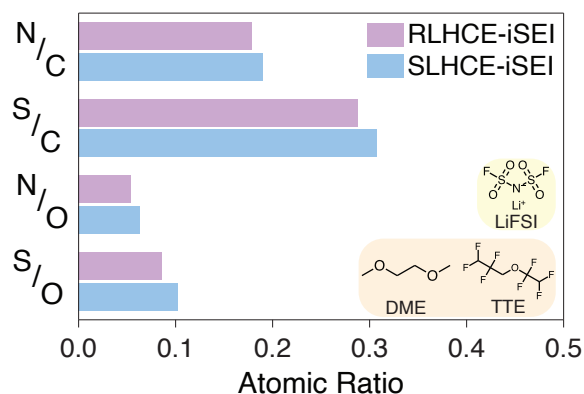
Supplementary Fig. 22. **a**, Low (left) and high (right) magnification SEM images of electrodeposited Li^0 on Cu with RLHCE at 1 mA cm^{-2} and 1 mAh cm^{-2} from $\text{Li}|\text{Cu}$ cell. The inset image shows the physical image of RLHCE. **b**, Low (left) and high (right) magnification SEM images of electrodeposited Li^0 on Cu with SLHCE at 1 mA cm^{-2} and 1 mAh cm^{-2} from $\text{Li}|\text{Cu}$ cell. The inset image shows the physical image of SLHCE.



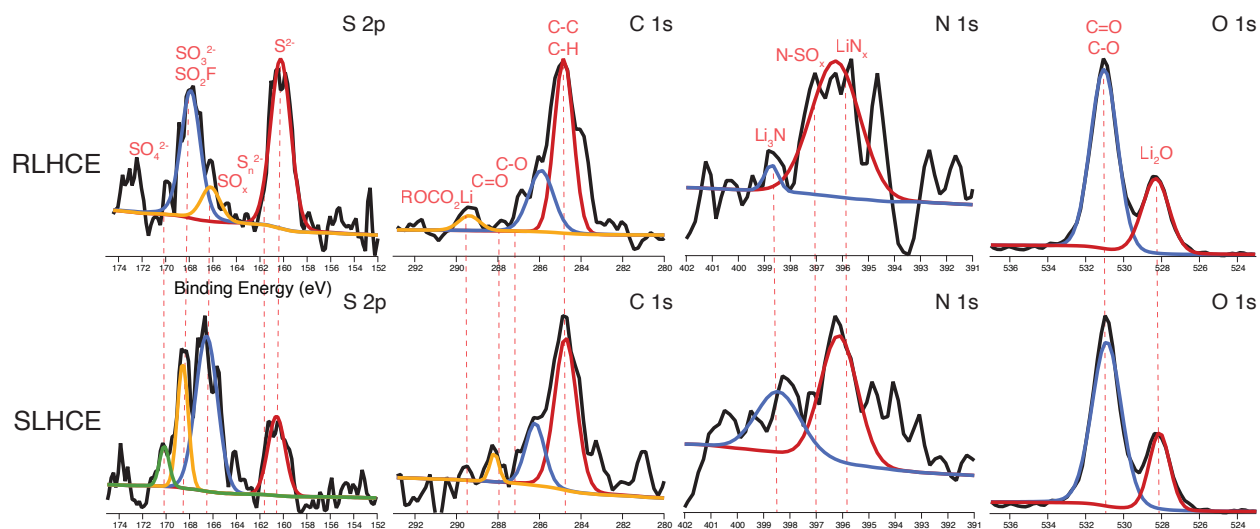
Supplementary Fig. 23. Elemental ratios of N/C, S/C, N/O, and S/O on RFE-iSEI and SFE-iSEI obtained from XPS scans. The XPS scans were performed on electrodeposited Li^0 on Cu from $\text{Li}|\text{Cu}$ cells with RFE and SFE at 1 mA cm^{-2} and 1 mAh cm^{-2} . The insets represent electrolyte species that can be reduced to form iSEIs on the electrodeposited Li^0 on Cu.



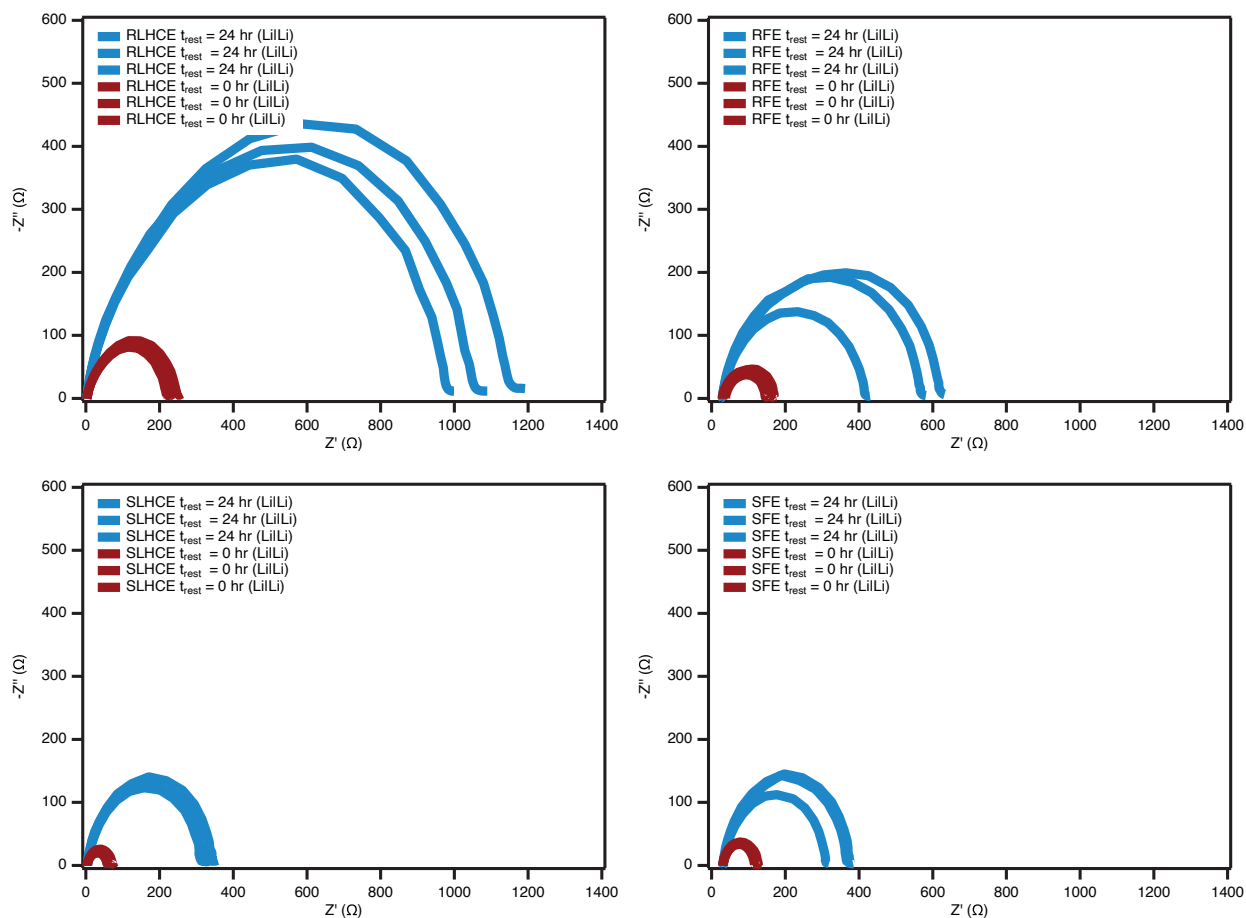
Supplementary Fig. 24. Narrow XPS scans of S, C, N, and O of the electrodeposited Li^0 on Cu from $\text{Li}|\text{Cu}$ cells with RFE and SFE.



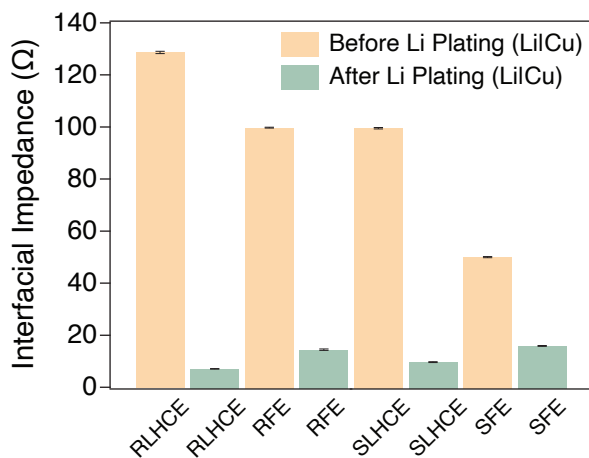
Supplementary Fig. 25. Elemental ratios of N/C, S/C, N/O, and S/O on RLHCE-iSEI and SLHCE-iSEI obtained from XPS scans. The XPS scans were performed on electrodeposited Li^0 on Cu from Li|Cu cells with RLHCE and SLHCE at 1 mA cm^{-2} and 1 mAh cm^{-2} . The insets represent electrolyte species that can be reduced to form iSEIs on the electrodeposited Li^0 on Cu.



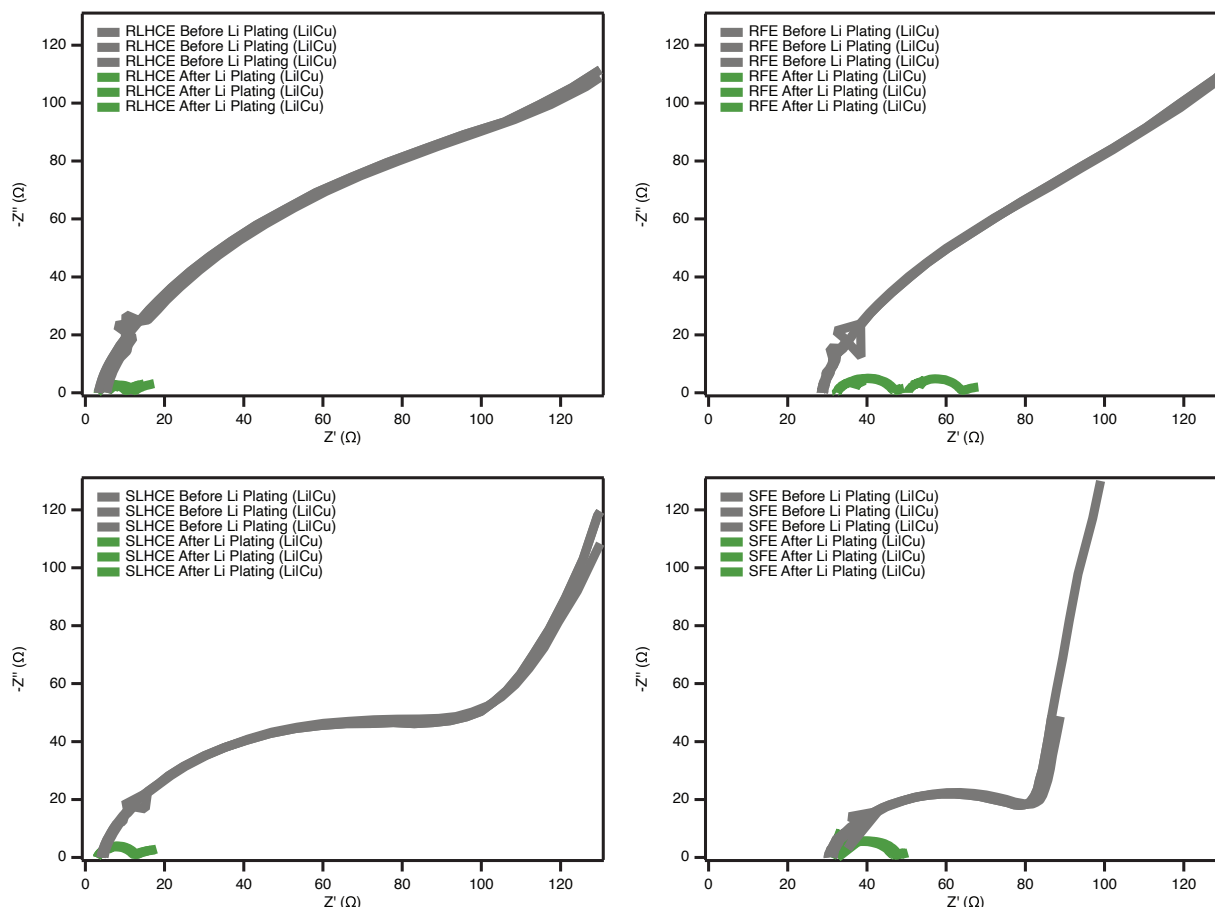
Supplementary Fig. 26. Narrow XPS scans of S, C, N, and O of the electrodeposited Li^0 on Cu from Li|Cu cells with RLHCE and SLHCE.



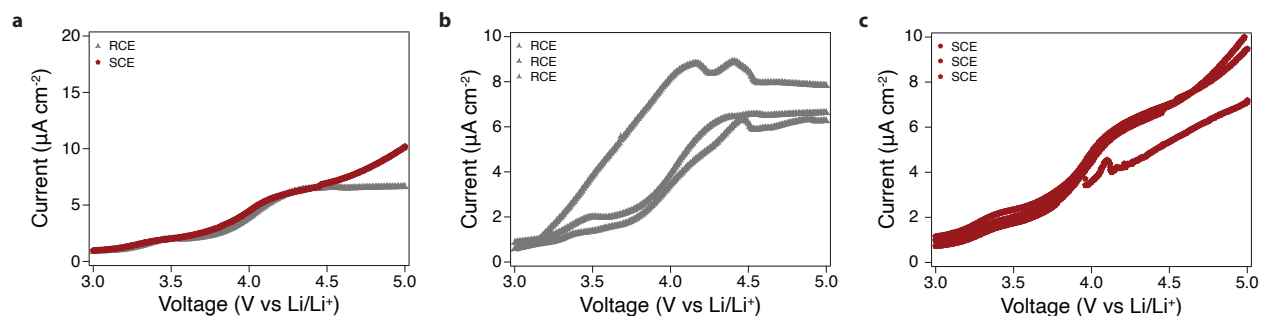
Supplementary Fig. 27. Nyquist plots of three identical Li|Li cells measured at $t_{\text{rest}} = 0$ hr and $t_{\text{rest}} = 24$ hr with RLHCE, RFE, SLHCE, and SFE. t_{rest} represents the cell resting time after the cell assembly.



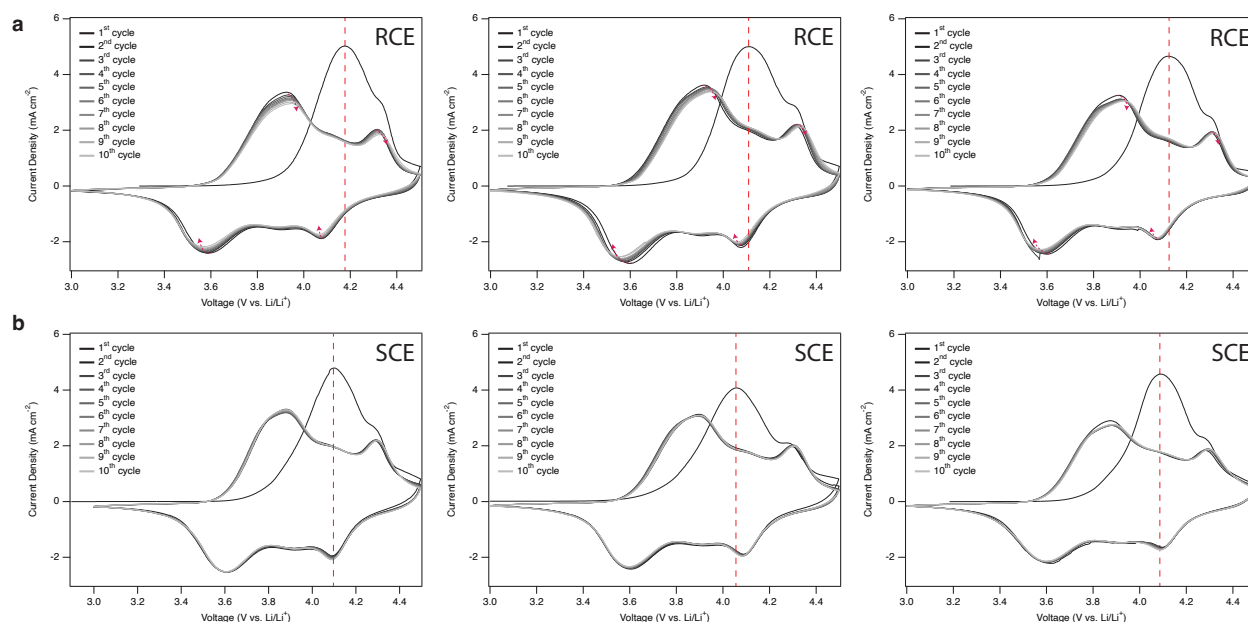
Supplementary Fig. 28. Measured interfacial impedance of three identical Li|Cu cells before and after $1 \text{ mAh cm}^{-2} \text{ Li}^0$ electrodeposition on Cu from Li|Cu cells with RLHCE, RFE, SLHCE, and SFE at 1 mA cm^{-2} .



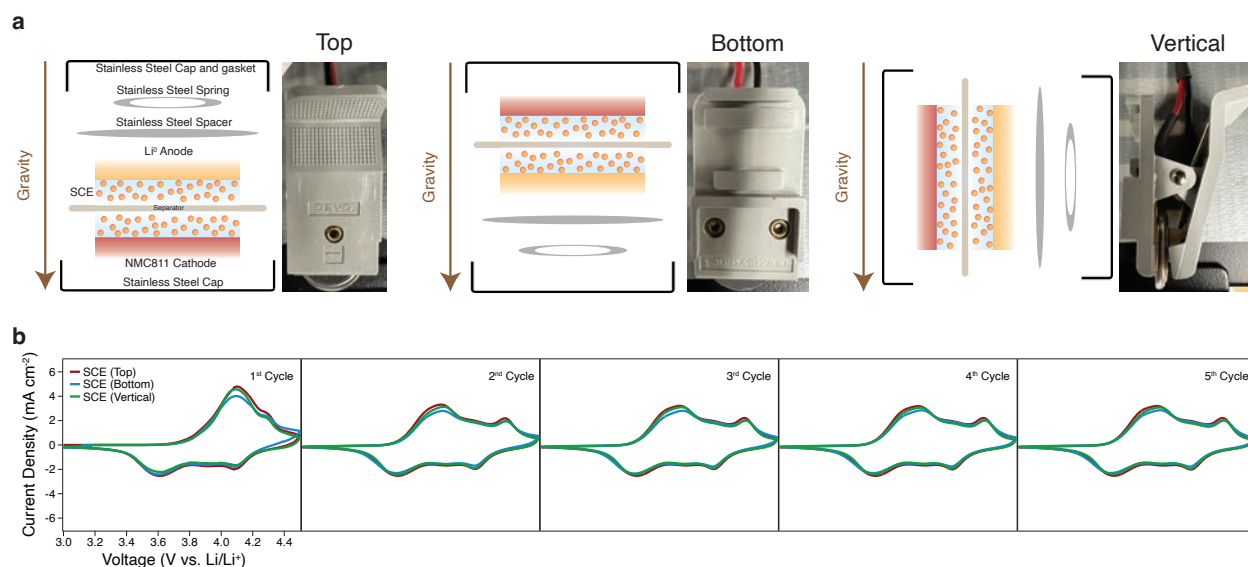
Supplementary Fig. 29. Nyquist plots of three identical Li|Cu cells measured before and after 1 mAh cm⁻² Li⁰ electrodeposited on Cu at 1 mA cm⁻² with RLHCE, RFE, SLHCE, and SFE.



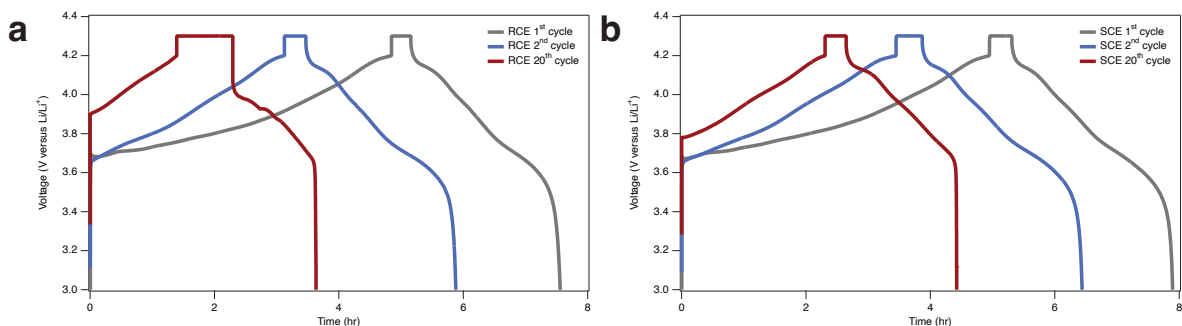
Supplementary Fig. 30. **a**, Representative linear sweep voltammetry (LSV) current density profiles of Li|Al cells with RCE and SCE. The scan rate and voltage window used were 1 mV s⁻¹ and 3 V to 5 V vs. Li/Li⁺. **b**, LSV current density profiles of three identical Li|Al cells with RCE. **c**, LSV current density profiles of three identical Li|Al cells with SCE.



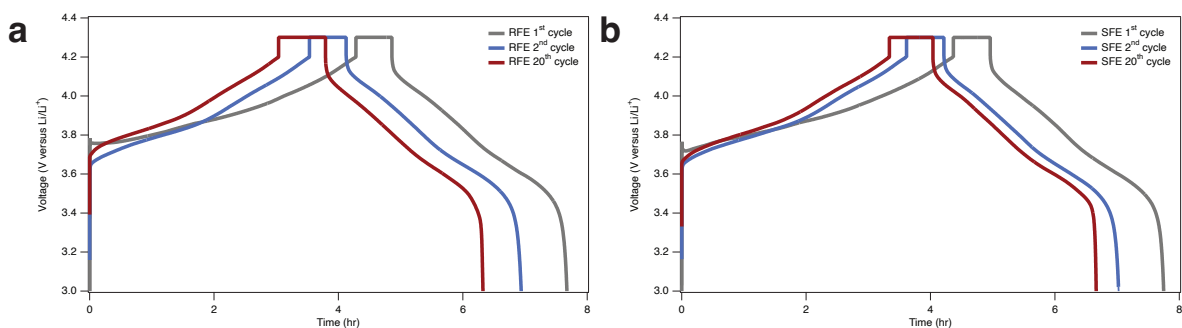
Supplementary Fig. 31. Cyclic voltammograms of three identical Li|NMC811 cells measured with RCE (a) and SCE (b). The scan rate and voltage window used were 0.1 mV s^{-1} and 3 V to 4.5 V vs. Li/Li^+ . The red dashed lines and arrows indicate the first redox potential at the current density peak in the 1st charging cycle and redox potential shifts during the first 10 cycles, respectively.



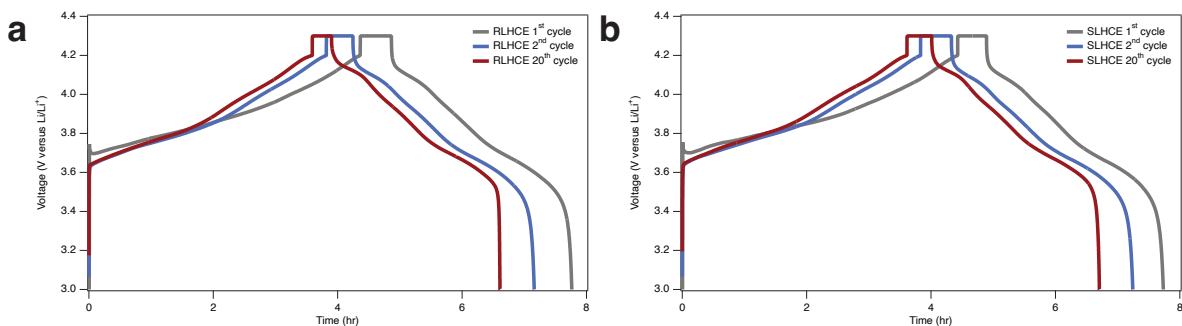
Supplementary Fig. 32. Gravity and cell orientation effects for SCE. a, Schematics for the direction of gravity and tested cell orientations. “Top” configuration represents the Li^0 anode located at the top of the cell. “Bottom” configuration represents the Li^0 anode located at the bottom of the cell. “Vertical” configuration represents the Li^0 anode being parallel to the direction of gravity. b, Cyclic voltammograms from the 1st cycle to the 5th cycle of Li|NMC811 cells tested at Top, Bottom, and Vertical cell orientations with SCE. The scan rate and voltage window used were 0.1 mV s^{-1} and 3 V to 4.5 V vs. Li/Li^+ .



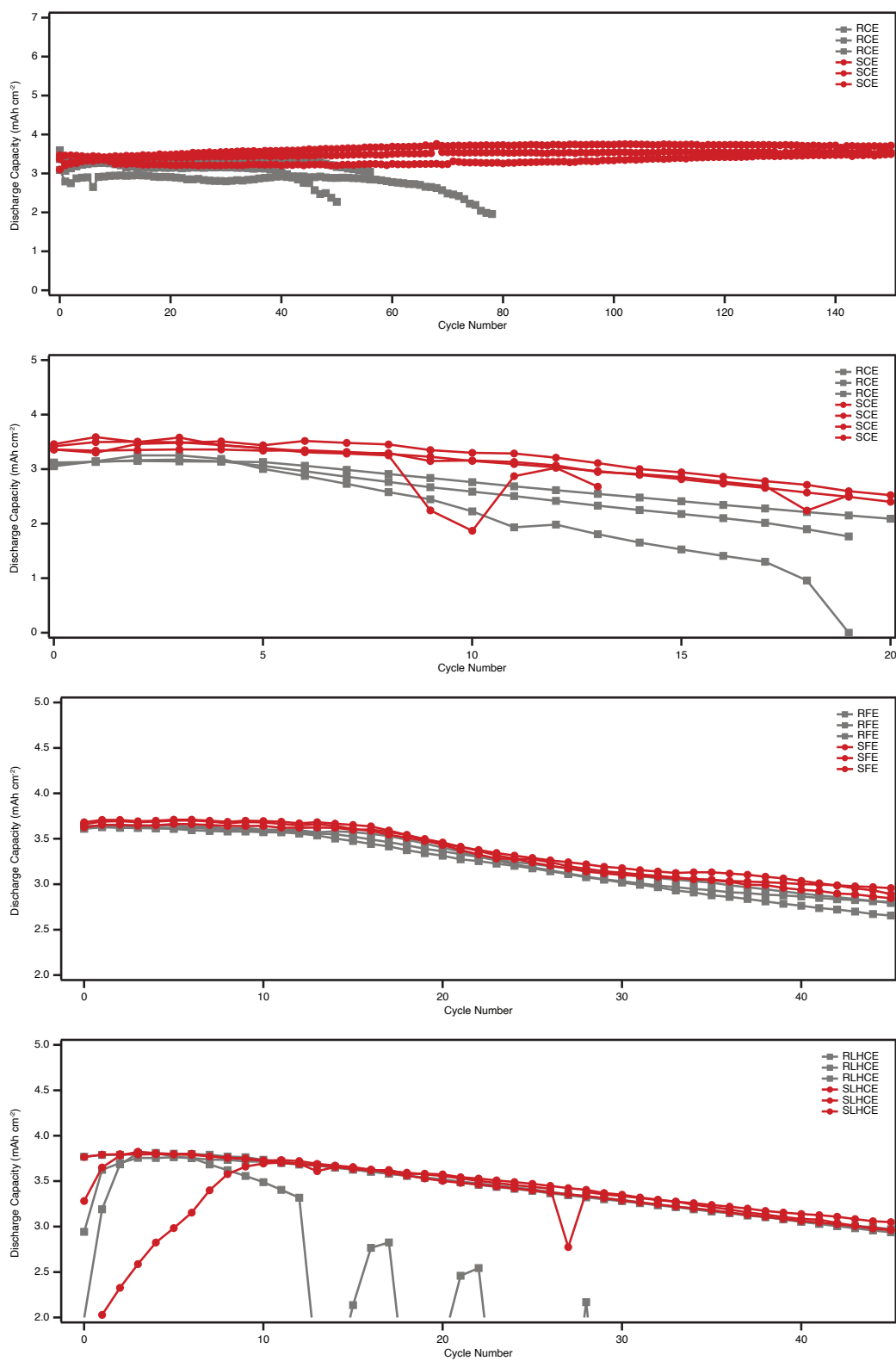
Supplementary Fig. 33. a, Charge/discharge voltage profiles of the anode-less Cu|NMC811 cell with RCE at the 1st, 2nd, and 20th cycles. The galvanostatic charging was executed from 3.0 V to 4.2 V vs. Li/Li⁺ at 0.2C with the constant voltage charging remaining at 4.3 V vs. Li/Li⁺ with cut-off current of 0.05C. The galvanostatic discharging was executed from 4.3 V to 3.0 V vs. Li/Li⁺ at 0.3C. **b**, Charge/discharge voltage profiles of the anode-less Cu|NMC811 cell with SCE at the 1st, 2nd, and 20th cycles.



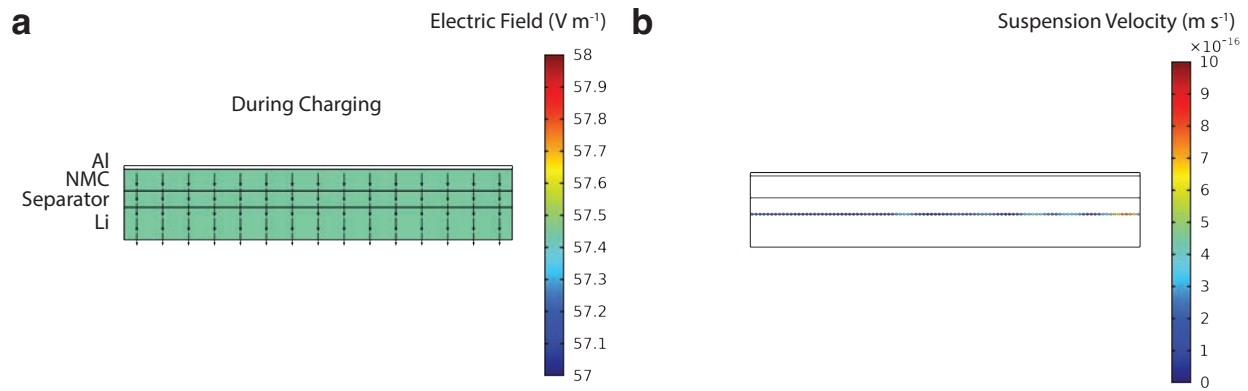
Supplementary Fig. 34. a, Charge/discharge voltage profiles of the anode-less Cu|NMC811 cell with RFE at the 1st, 2nd, and 20th cycles. The galvanostatic charging was executed from 3.0 V to 4.2 V vs. Li/Li⁺ at 0.2C with the constant voltage charging remaining at 4.3 V vs. Li/Li⁺ with cut-off current of 0.05C. The galvanostatic discharging was executed from 4.3 V to 3.0 V vs. Li/Li⁺ at 0.3C. **b**, Charge/discharge voltage profiles of the anode-less Cu|NMC811 cell with SFE at the 1st, 2nd, and 20th cycles.



Supplementary Fig. 35. a, Charge/discharge voltage profiles of the anode-less Cu|NMC811 cell with RLHCE at the 1st, 2nd, and 20th cycles. The galvanostatic charging was executed from 3.0 V to 4.2 V vs. Li/Li⁺ at 0.2C with the constant voltage charging remaining at 4.3 V vs. Li/Li⁺ with the cut-off current of 0.05C. The galvanostatic discharging was executed from 4.3 V to 3.0 V vs. Li/Li⁺ at 0.3C. **b**, Charge/discharge voltage profiles of the anode-less Cu|NMC811 cell with SLHCE at the 1st, 2nd, and 20th cycles.



Supplementary Fig. 36. Full cell (Li|NMC811 and Cu|NMC811) capacity retention profiles measured from the three cells with each of the reference (RCE, RFE, and RLHCE) and suspension (SCE, SFE, and SLHCE) electrolytes. The cycling profiles are displayed in the same manner as reported in Fig. 6.



Supplementary Fig. 37. a, Finite element analysis on the electrical potential field generated from the electrodes in Li|NMC cell. **b**, Finite element analysis on the Li_2O suspension particle velocities projected from the Li|NMC cell under the electrical potential fields in **(a)**.

SUPPLEMENTARY TABLES

| Li ₂ O contents (%) | Li Li (t _{rest} = 0 hr) | Li Cu (t _{rest} = 0 hr) |
|--------------------------------|----------------------------------|----------------------------------|
| 0% | 200.715 | 203.834 |
| 0% | 191.940 | 229.237 |
| 0% | 185.105 | 209.489 |
| Mean | 192.586 | 214.186 |
| Error | 3.688 | 6.287 |
| 1% | 105.672 | 98.098 |
| 1% | 110.625 | 97.410 |
| 1% | 108.465 | 101.056 |
| Mean | 108.254 | 98.854 |
| Error | 1.171 | 0.913 |
| 3% | 86.575 | 81.796 |
| 3% | 86.010 | 79.485 |
| 3% | 81.9195 | 78.866 |
| Mean | 84.834 | 80.049 |
| Error | 1.197 | 0.728 |
| 7% | 63.418 | 65.939 |
| 7% | 62.419 | 59.358 |
| 7% | 61.198 | 62.579 |
| Mean | 62.345 | 62.625 |
| Error | 0.524 | 1.551 |
| 10% | 60.581 | 54.838 |
| 10% | 59.652 | 56.084 |
| 10% | 59.597 | 53.239 |
| Mean | 59.943 | 54.720 |
| Error | 0.261 | 0.672 |
| 20% | 52.422 | 54.837 |
| 20% | 49.247 | 51.268 |
| 20% | 49.887 | 48.759 |
| Mean | 50.518 | 51.621 |
| Error | 0.791 | 1.439 |

Supplementary Table 1. Averaged interfacial impedance values of Li|Li and Li|Cu cells with the Li₂O nanoparticle suspension ranging from 0 wt% to 20 wt% in RCE measured at t_{rest} = 0 hr with standard errors obtained from three identical Li|Li and Li|Cu cells for each of the Li₂O suspension contents (0 wt%, 1 wt%, 3 wt%, 7 wt%, 10 wt%, and 20 wt% Li₂O). t_{rest} represents the cell resting time after the cell assembly.

| Li₂O contents (%) | Li Li (t_{rest} = 0 hr) | Li Li (t_{rest} = 24 hr) |
|-------------------------------------|--|---|
| 0% | 200.715 | 670.939 |
| 0% | 191.940 | 628.711 |
| 0% | 185.105 | 486.755 |
| Mean | 192.586 | 595.468 |
| Error | 3.688 | 45.484 |
| 1% | 105.672 | 128.509 |
| 1% | 110.625 | 122.710 |
| 1% | 108.465 | 119.873 |
| Mean | 108.254 | 123.697 |
| Error | 1.171 | 2.075 |
| 3% | 86.575 | 93.491 |
| 3% | 86.010 | 92.352 |
| 3% | 81.9195 | 90.699 |
| Mean | 84.834 | 92.181 |
| Error | 1.197 | 0.662 |
| 7% | 63.418 | 70.068 |
| 7% | 62.419 | 68.927 |
| 7% | 61.198 | 64.762 |
| Mean | 62.345 | 67.919 |
| Error | 0.524 | 1.316 |
| 10% | 60.581 | 61.853 |
| 10% | 59.652 | 61.967 |
| 10% | 59.597 | 59.859 |
| Mean | 59.943 | 61.226 |
| Error | 0.261 | 0.559 |
| 20% | 52.422 | 53.222 |
| 20% | 49.247 | 52.770 |
| 20% | 49.887 | 50.232 |
| Mean | 50.518 | 52.075 |
| Error | 0.791 | 0.759 |

Supplementary Table 2. Averaged interfacial impedance values of Li|Li cells with the Li₂O nanoparticle suspension ranging from 0 wt% to 20 wt% in RCE measured at t_{rest} = 0 hr and at t_{rest} = 24 hr with standard errors obtained from three identical Li|Li cells for each of the Li₂O suspension contents (0 wt%, 1 wt%, 3 wt%, 7 wt%, 10 wt%, and 20 wt% Li₂O). t_{rest} represents the cell resting time after the cell assembly.

| Electrolyte | Li Cu (Before Li ⁰ deposition) | Li Cu (After Li ⁰ deposition) |
|--------------|---|--|
| RCE | 203.834 | 47.608 |
| RCE | 229.237 | 41.909 |
| RCE | 209.489 | 40.776 |
| Mean | 214.187 | 43.431 |
| Error | 6.287 | 1.726 |
| SCE | 65.939 | 45.876 |
| SCE | 59.358 | 47.581 |
| SCE | 62.579 | 27.869 |
| Mean | 62.625 | 40.442 |
| Error | 1.551 | 5.149 |

Supplementary Table 3. Averaged interfacial impedance values of Li|Cu cells with RCE and SCE measured before and after 1 mAh cm⁻² Li⁰ deposition on Cu with standard errors obtained from three identical Li|Cu cells for each of the electrolytes (RCE and SCE).

| Measurements | SFE | RFE | SLHCE | RLHCE |
|---|--------------|--------------|--------------|--------------|
| CE (%) | 99.70 | 99.48 | 99.59 | 99.49 |
| CE (%) | 99.63 | 99.54 | 99.51 | 99.42 |
| CE (%) | 99.65 | 99.51 | 99.49 | 99.35 |
| CE (%) | 99.62 | 99.55 | 99.57 | 99.48 |
| Averaged CE (%) | 99.65 | 99.52 | 99.54 | 99.43 |
| CE Standard Error (%) | 0.014 | 0.015 | 0.020 | 0.030 |
| | | | | |
| Nucleation overpotential (mV) | 76.88 | 96.11 | 47.17 | 99.81 |
| Nucleation overpotential (mV) | 78.43 | 56.73 | 82.72 | 102.29 |
| Nucleation overpotential (mV) | 78.68 | 73.37 | 65.53 | 85.03 |
| Nucleation overpotential (mV) | 76.52 | 92.07 | 78.07 | 73.96 |
| Averaged Nucleation overpotential (mV) | 77.63 | 79.57 | 68.37 | 90.27 |
| Nucleation overpotential Standard Error (mV) | 0.47 | 7.87 | 6.88 | 5.75 |

Supplementary Table 4. Averaged CE and the nucleation overpotential values of SFE, RFE, SLHCE, and RLHCE with standard errors obtained from four identical cells for each of the electrolytes (SFE, RFE, SLHCE, and RLHCE).

| Electrolyte | Li Cu (Before Li ⁰ deposition) | Li Cu (After Li ⁰ deposition) |
|--------------|---|--|
| RLHCE | 127.634 | 6.860 |
| RLHCE | 129.075 | 7.374 |
| RLHCE | 129.358 | 6.980 |
| Mean | 128.689 | 7.0715 |
| Error | 0.436 | 0.127 |
| RFE | 99.394 | 13.853 |
| RFE | 99.857 | 14.888 |
| RFE | 100.1375 | 14.744 |
| Mean | 99.7963 | 14.495 |
| Error | 0.177 | 0.264 |
| SLHCE | 100.195 | 10.024 |
| SLHCE | 99.0805 | 9.756 |
| SLHCE | 99.352 | 9.312 |
| Mean | 99.5425 | 9.697 |
| Error | 0.274 | 0.1695 |
| SFE | 50.385 | 15.906 |
| SFE | 49.535 | 16.1885 |
| SFE | 50.173 | 15.599 |
| Mean | 50.031 | 15.898 |
| Error | 0.2085 | 0.139 |

Supplementary Table 5. Averaged interfacial impedance values of Li|Cu cells with RLHCE, RFE, SLHCE, and SFE measured before and after 1 mAh cm⁻² Li⁰ deposition on Cu with standard errors obtained from three identical Li|Cu cells for each of the electrolytes (RLHCE, RFE, SLHCE, and SFE).

SUPPLEMENTARY REFERENCES

1. Wu, H., Jia, H., Wang, C., Zhang, J. G. & Xu, W. Recent Progress in Understanding Solid Electrolyte Interphase on Lithium Metal Anodes. *Adv. Energy Mater.* **11**, 1–35 (2021).
2. Yamada, Y., Wang, J., Ko, S., Watanabe, E. & Yamada, A. Advances and issues in developing salt-concentrated battery electrolytes. *Nat. Energy* **4**, 269–280 (2019).
3. Yu, Z., Wang, H., Kong, X., Huang, W., Tsao, Y., Mackanic, D. G., Wang, K., Wang, X., Huang, W., Choudhury, S., Zheng, Y., Amanchukwu, C. V., Hung, S. T., Ma, Y., Lomeli, E. G., Qin, J., Cui, Y. & Bao, Z. Molecular design for electrolyte solvents enabling energy-dense and long-cycling lithium metal batteries. *Nat. Energy* **5**, 526–533 (2020).
4. Ren, X., Zou, L., Cao, X., Engelhard, M. H., Liu, W., Burton, S. D., Lee, H., Niu, C., Matthews, B. E., Zhu, Z., Wang, C., Arey, B. W., Xiao, J., Liu, J., Zhang, J. G. & Xu, W. Enabling High-Voltage Lithium-Metal Batteries under Practical Conditions. *Joule* **3**, 1662–1676 (2019).
5. Ren, X., Chen, S., Lee, H., Mei, D., Engelhard, M. H., Burton, S. D., Zhao, W., Zheng, J., Li, Q., Ding, M. S., Schroeder, M., Alvarado, J., Xu, K., Meng, Y. S., Liu, J., Zhang, J. G. & Xu, W. Localized High-Concentration Sulfone Electrolytes for High-Efficiency Lithium-Metal Batteries. *Chem* **4**, 1877–1892 (2018).
6. Soto, F. A., Ma, Y., Martinez De La Hoz, J. M., Seminario, J. M. & Balbuena, P. B. Formation and Growth Mechanisms of Solid-Electrolyte Interphase Layers in Rechargeable Batteries. *Chem. Mater.* **27**, 7990–8000 (2015).
7. Boyle, D. T., Huang, W., Wang, H., Li, Y., Chen, H., Yu, Z., Zhang, W., Bao, Z. & Cui, Y. Corrosion of lithium metal anodes during calendar ageing and its microscopic origins. *Nat. Energy* (2021). doi:10.1038/s41560-021-00787-9
8. Tasaki, K., Goldberg, A., Lian, J.-J., Walker, M., Timmons, A. & Harris, S. J. Solubility of Lithium Salts Formed on the Lithium-Ion Battery Negative Electrode Surface in Organic Solvents. *J. Electrochem. Soc.* **156**, A1019 (2009).
9. Wang, L., Menakath, A., Han, F., Wang, Y., Zavalij, P. Y., Gaskell, K. J., Borodin, O., Iuga, D., Brown, S. P., Wang, C., Xu, K. & Eichhorn, B. W. Identifying the components of the solid–electrolyte interphase in Li-ion batteries. *Nat. Chem.* **11**, 789–796 (2019).
10. Zachman, M. J., Tu, Z., Choudhury, S., Archer, L. A. & Kourkoutis, L. F. Cryo-STEM mapping of solid–liquid interfaces and dendrites in lithium-metal batteries. *Nature* **560**, 345–349 (2018).
11. Huang, W., Wang, H., Boyle, D. T., Li, Y. & Cui, Y. Resolving Nanoscopic and Mesoscopic Heterogeneity of Fluorinated Species in Battery Solid-Electrolyte Interphases by Cryogenic Electron Microscopy. *ACS Energy Lett.* **5**, 1128–1135 (2020).
12. Brown, Z. L., Jung, S., Nguyen, C. C. & Lucht, B. L. Effect of Fluoroethylene Carbonate Electrolytes on the Nanostructure of the Solid Electrolyte Interphase and Performance of Lithium Metal Anodes. *ACS Appl. Energy Mater.* **1**, 3057–3062 (2018).
13. Ramasubramanian, A., Yurkiv, V., Foroozan, T., Ragone, M., Shahbazian-Yassar, R. & Mashayek, F. Stability of solid-electrolyte interphase (SEI) on the lithium metal surface in lithium metal batteries (LMBs). *ACS Appl. Energy Mater.* **3**, 10560–10567 (2020).
14. Ramasubramanian, A., Yurkiv, V., Foroozan, T., Ragone, M., Shahbazian-Yassar, R. & Mashayek, F. Lithium Diffusion Mechanism through Solid-Electrolyte Interphase in Rechargeable Lithium Batteries. *J. Phys. Chem. C* **123**, 10237–10245 (2019).
15. Benitez, L. & Seminario, J. M. Ion Diffusivity through the Solid Electrolyte Interphase in Lithium-Ion Batteries. *J. Electrochem. Soc.* **164**, E3159–E3170 (2017).

16. Lu, Y., Tu, Z. & Archer, L. A. Stable lithium electrodeposition in liquid and nanoporous solid electrolytes. *Nat. Mater.* **13**, 961–969 (2014).
17. Li, Y., Huang, W., Li, Y., Pei, A., Boyle, D. T. & Cui, Y. Correlating Structure and Function of Battery Interphases at Atomic Resolution Using Cryoelectron Microscopy. *Joule* **2**, 2167–2177 (2018).
18. Li, Y., Li, Y., Pei, A., Yan, K., Sun, Y., Wu, C. L., Joubert, L. M., Chin, R., Koh, A. L., Yu, Y., Perrino, J., Butz, B., Chu, S. & Cui, Y. Atomic structure of sensitive battery materials and interfaces revealed by cryo–electron microscopy. *Science*. **358**, 506–510 (2017).
19. Cao, X., Ren, X., Zou, L., Engelhard, M. H., Huang, W., Wang, H., Matthews, B. E., Lee, H., Niu, C., Arey, B. W., Cui, Y., Wang, C., Xiao, J., Liu, J., Xu, W. & Zhang, J.-G. Monolithic solid–electrolyte interphases formed in fluorinated orthoformate-based electrolytes minimize Li depletion and pulverization. *Nat. Energy* **4**, 796–805 (2019).
20. Ozhabes, Y., Gunceler, D. & Arias, T. A. Stability and surface diffusion at lithium-electrolyte interphases with connections to dendrite suppression. *arXiv:1504.05799* 1–7 (2015). at <<http://arxiv.org/abs/1504.05799>>
21. Kim, M. S., Lee, S. H., Kim, M.-S., Ryu, J.-H., Lee, K.-R., Archer, L. A. & Cho, W. II. *Enabling reversible redox reactions in electrochemical cells using protected LiAl intermetallics as lithium metal anodes.* *Sci. Adv.* **5**, (2019).
22. Guo, R. & Gallant, B. M. Li₂O Solid Electrolyte Interphase: Probing Transport Properties at the Chemical Potential of Lithium. *Chem. Mater.* (2020). doi:10.1021/acs.chemmater.0c00333
23. Kim, S. C., Kong, X., Vilá, R. A., Huang, W., Chen, Y., Boyle, D. T., Yu, Z., Wang, H., Bao, Z., Qin, J. & Cui, Y. Potentiometric Measurement to Probe Solvation Energy and Its Correlation to Lithium Battery Cyclability. *J. Am. Chem. Soc.* **143**, 10301–10308 (2021).
24. Xie, J., Sendek, A. D., Cubuk, E. D., Zhang, X., Lu, Z., Gong, Y., Wu, T., Shi, F., Liu, W., Reed, E. J. & Cui, Y. Atomic Layer Deposition of Stable LiAlF₄ Lithium Ion Conductive Interfacial Layer for Stable Cathode Cycling. *ACS Nano* **11**, 7019–7027 (2017).
25. Liu, Y., Lin, D., Li, Y., Chen, G., Pei, A., Nix, O., Li, Y. & Cui, Y. Solubility-mediated sustained release enabling nitrate additive in carbonate electrolytes for stable lithium metal anode. *Nat. Commun.* **9**, 1–10 (2018).
26. Wang, J., Huang, W., Pei, A., Li, Y., Shi, F., Yu, X. & Cui, Y. Improving cyclability of Li metal batteries at elevated temperatures and its origin revealed by cryo–electron microscopy. *Nat. Energy* **4**, 664–670 (2019).
27. Lowe, J. S. & Siegel, D. J. Modeling the Interface between Lithium Metal and Its Native Oxide. *ACS Appl. Mater. Interfaces* **12**, 46015–46026 (2020).
28. Tan, L., Li, X., Cheng, M., Liu, T., Wang, Z., Guo, H., Yan, G., Li, L., Liu, Y. & Wang, J. In-situ tailored 3D Li₂O@Cu nanowires array enabling stable lithium metal anode with ultra-high coulombic efficiency. *J. Power Sources* **463**, 228178 (2020).
29. Shen, C., Yan, H., Gu, J., Gao, Y., Yang, J. & Xie, K. Li₂O-reinforced solid electrolyte interphase on three-dimensional sponges for dendrite-free lithium deposition. *Front. Chem.* **6**, 1–9 (2018).
30. Yuan, S., Bao, J. L., Wang, N., Zhang, X., Wang, Y., Truhlar, D. G. & Xia, Y. Salt-rich solid electrolyte interphase for safer high-energy-density Li metal batteries with limited Li excess. *Chem. Commun.* **56**, 8257–8260 (2020).

31. Fan, X., Chen, L., Ji, X., Deng, T., Hou, S., Chen, J., Zheng, J., Wang, F., Jiang, J., Xu, K. & Wang, C. Highly Fluorinated Interphases Enable High-Voltage Li-Metal Batteries. *Chem* **4**, 174–185 (2018).
32. Qian, J., Henderson, W. A., Xu, W., Bhattacharya, P., Engelhard, M., Borodin, O. & Zhang, J. G. High rate and stable cycling of lithium metal anode. *Nat. Commun.* **6**, (2015).
33. Suo, L., Borodin, O., Gao, T., Olguin, M., Ho, J., Fan, X., Luo, C., Wang, C. & Xu, K. ‘Water-in-salt’ electrolyte enables high-voltage aqueous lithium-ion chemistries. *Science*. **350**, 938–943 (2015).
34. Chen, S., Zheng, J., Mei, D., Han, K. S., Engelhard, M. H., Zhao, W., Xu, W., Liu, J. & Zhang, J. G. High-Voltage Lithium-Metal Batteries Enabled by Localized High-Concentration Electrolytes. *Adv. Mater.* **30**, (2018).
35. Chen, S., Zheng, J., Yu, L., Ren, X., Engelhard, M. H., Niu, C., Lee, H., Xu, W., Xiao, J., Liu, J. & Zhang, J. G. High-Efficiency Lithium Metal Batteries with Fire-Retardant Electrolytes. *Joule* **2**, 1548–1558 (2018).
36. Heiskanen, S. K., Kim, J. & Lucht, B. L. Generation and Evolution of the Solid Electrolyte Interphase of Lithium-Ion Batteries. *Joule* **3**, 2322–2333 (2019).